

Molecular gas content in obscured AGN at $z > 1$

M. Perna^{1,2}, M. T. Sargent³, M. Brusa^{2,4}, E. Daddi⁵, C. Feruglio⁶, G. Cresci¹, G. Lanzuisi^{2,4}, E. Lusso⁷,
A. Comastri⁴, R. T. Coogan³, Q. D’Amato², R. Gilli⁶, E. Piconcelli⁸, and C. Vignali^{2,4}

¹ INAF – Osservatorio Astrofisico di Arcetri, Largo Enrico Fermi 5, 50125 Firenze, Italy
e-mail: perna@arcetri.inaf.it

² Dipartimento di Fisica e Astronomia, Università di Bologna, via Gobetti 93/2, 40129 Bologna, Italy

³ Astronomy Centre, Department of Physics and Astronomy, University of Sussex, Brighton BN1 9QH, UK

⁴ INAF Osservatorio di Astrofisica e Scienza dello Spazio di Bologna, via Gobetti 93/3, 40129 Bologna, Italy

⁵ CEA, IRFU, DAP, AIM, Université Paris-Saclay, Université Paris Diderot, Sorbonne Paris Cité, CNRS, 91191 Gif-sur-Yvette, France

⁶ INAF Osservatorio Astronomico di Trieste, Via G.B. Tiepolo 11, 34143 Trieste, Italy

⁷ Centre for Extragalactic Astronomy, Department of Physics, Durham University, South Road, Durham DH1 3LE, UK

⁸ INAF – Osservatorio Astronomico di Roma, via Frascati 33, 00078 Monte Porzio Catone, Rome, Italy

Received 18 March 2018 / Accepted 7 July 2018

ABSTRACT

Aims. The standard active galactic nuclei (AGN)-galaxy co-evolutionary scenario predicts a phase of deeply “buried” supermassive black hole growth coexisting with a starburst (SB) before feedback phenomena deplete the cold molecular gas reservoir of the galaxy and an optically luminous quasar (QSO) is revealed (called the SB-QSO evolutionary sequence). The aim of this work is to measure the cold gas reservoir of three highly obscured QSOs to test if their gas fraction is similar to that of submillimetre galaxies (SMGs), as expected by some models, and to place these measurements in the context of the SB-QSO framework.

Methods. We target CO(1-0) transition in BzK4892, a Compton thick (CT) QSO at $z = 2.6$, CO(1-0) in BzK8608 and CO(2-1) in CDF153, two highly obscured ($N_{\text{H}} \approx 6 \times 10^{23} \text{ cm}^{-2}$) QSOs at $z = 2.5$ and $z = 1.5$, respectively. For these targets, we place 3σ upper limits on the CO lines, with $L'_{\text{CO}} < (1.5 \div 2.8) \times 10^{10} \text{ K km s}^{-1} \text{ pc}^2$. We also compare the molecular gas conditions of our targets with those of other systems at $z > 1$, considering normal star-forming galaxies and SMGs, and unobscured and obscured AGN from the literature. For the AGN samples, we provide an updated and almost complete collection of targets with CO follow-up at $z > 1$.

Results. BzK4892 displays a high star formation efficiency ($\text{SFE} = L_{\text{IR}}/L'_{\text{CO}} > 410 L_{\odot}/(\text{K km s}^{-1} \text{ pc}^2)$) and a gas fraction $f_{\text{gas}} = M_{\text{gas}}/(M_{\text{star}} + M_{\text{gas}}) < 10\%$. Less stringent constraints are derived for the other two targets ($f_{\text{gas}} < 0.5$ and $\text{SFE} > 10 L_{\odot}/(\text{K km s}^{-1} \text{ pc}^2)$). From the comparison with the literature data we found that, on average, i) obscured AGN at $z > 1$ are associated with higher SFE and lower f_{gas} with respect to normal star-forming galaxies and SMGs; ii) mildly and highly obscured active galaxies have comparable gas fractions; iii) the SFE of CT and obscured AGN are similar to those of unobscured AGN.

Conclusions. Within the SB-QSO framework, these findings could be consistent with a scenario where feedback can impact the host galaxy already from the early phases of the SB-QSO evolutionary sequence.

Key words. galaxies: active – quasars: emission lines – galaxies: evolution – galaxies: ISM

1. Introduction

The observed scaling relations between the properties of supermassive black holes (SMBHs) and galaxies found in the local Universe suggest a close connection between the galaxy evolution and the growth of the central SMBH (see [Kormendy & Ho 2013](#) for a recent review). Both theoretical and observational arguments (e.g. [Alexander et al. 2005](#); [Hopkins et al. 2008](#); [Menci et al. 2008](#)) support a picture, first presented by [Sanders et al. \(1988\)](#), where a dusty, starburst (SB)-dominated system arising from a merger evolves into an optically luminous quasar (QSO). The QSO phase would emerge after the accreting SMBH experienced the “feedback” phase (see e.g. [Hopkins et al. 2008](#)), invoked to reproduce the host galaxy-SMBH scaling relations (but see also e.g. [Jahnke & Macciò 2011](#)). During this feedback phase, the active galactic nucleus (AGN) releases radiative and kinetic energy in the form of powerful outflowing winds which may be capable of clearing the entire galaxy of dust and gas thereby causing star formation

in the host to cease (see [Somerville & Davé 2015](#) for a recent review). We refer to this evolutionary picture as the SB-QSO evolutionary sequence.

In the past decade, the properties of cold molecular gas reservoirs of galaxies have been the subject of intense investigation. This gas phase is regarded as the immediate fuel from which stars form, and can be used to test the SB-QSO evolutionary sequence (e.g. [Kennicutt & Evans 2012](#); [Leroy et al. 2008](#)). Molecular gas studies, mostly involving observations of carbon monoxide (CO) emission lines, have been carried out in SB-dominated galaxies (e.g. ultra-luminous infrared galaxies, ULIRGs, at low redshift, and submillimetre galaxies, SMGs, at higher redshift), unobscured QSOs, and in normal star-forming galaxies (SFGs; e.g. [Carilli & Walter 2013](#); [Daddi et al. 2010](#); [Tacconi et al. 2013](#); [Aravena et al. 2014](#)). These studies show that optically luminous QSOs are characterised by low molecular gas content with respect to their current star formation rate (SFR), or alternatively by high star formation efficiency (SFE), defined as the rate of star formation per unit of molecular gas

mass, $SFE = SFR/M_{\text{gas}}$ or $SFE = L_{\text{IR}}/L'_{\text{CO}}{}^1$, in the range between a few $100 L_{\odot}/(\text{K km s}^{-1} \text{ pc}^2)$ (units omitted from now on for simplicity) and ≈ 1000 (see e.g. Fig. 4 in Feruglio et al. 2014 for an early compilation). On the other hand, normal star-forming galaxies and SBs display SFE values in the range from ~ 10 to 200, with the latter population generally lying at the upper end of this range (Feruglio et al. 2014). We note that the SFE of individual classes of sources is roughly constant with redshift at $z > 1$ (e.g. Sargent et al. 2014; Feruglio et al. 2014; Schinnerer et al. 2016; Tacconi et al. 2018; Yang et al. 2017). Therefore, the characteristic SFE-ranges for optically luminous QSOs and star-forming galaxies quoted above are effectively applicable at all $z > 1$ (see Sect. 4.1 for more detailed discussion).

According to the SB-QSO paradigm, the SFE of unobscured QSOs should be significantly higher than for main sequence (MS; Speagle et al. 2014) galaxies and SBs because of the AGN feedback which expelled the gas from their host galaxies during previous phases. In particular, during the initial stages of the merger, the SFR is expected to be a factor of a few higher (up to 10) with respect to normal, isolated galaxies (Di Matteo et al. 2005, 2007; Hopkins 2012). This translates to an enhancement of the SFE by the same amount (Di Matteo et al. 2007). An even higher SFE could be associated with the subsequent phases, i.e. the feedback phase and in particular the QSO phase, because the CO luminosity reflects the current (depleted) amount of molecular gas, while the IR emission responds to the associated decrease in SF more slowly than the outflow timescales (see Sect. 2; Fig. 1).

In the SB-QSO evolutionary sequence, obscured AGN are associated with a transitioning phase between the SB- and QSO-dominated stages so that the higher the obscuration, the larger the gas reservoirs in the host galaxy. In this framework, the obscuration is due to galaxy-scale absorbers rather than a nuclear dusty torus on the line of sight. Although this argument is still debated and might not be applicable to all the obscured systems, there is some observational evidence confirming the presence of galaxy-scale absorbers in obscured QSOs (see e.g. Lanzuisi et al. 2017 and references therein; Gallerani et al. 2017; Gilli et al. 2010, 2014; Rosario et al. 2018; Symeonidis 2017). This is suggested, for example, by the correlation between the nuclear column density (N_{H}) and the amount of gas traced by the CO on kpc-scales (e.g. Rosario et al. 2018), and by the fact that in a few high- z CT AGN the absorber can be fully accounted for by the amount of CO gas and its compactness (e.g. Gilli et al. 2014). Moreover, numerical simulations by Hopkins et al. (2016) also show that typical nuclear conditions of post-merger objects are generally associated with isotropically obscured SMBHs with $\log(N_{\text{H}}/\text{cm}^{-2}) \approx 24 - 26$. Only when the AGN-driven winds start, a cavity is generated in the direction perpendicular to SMBH accretion disk and the nuclear regions can be observed as a mildly-to-modestly obscured AGN (see also e.g. Hopkins 2005).

The study of the molecular gas conditions in different classes of sources may play an important role to test the SB-QSO evolutionary sequence. In this regard, scarce observations have been carried out for heavily obscured AGN at the peak epoch of

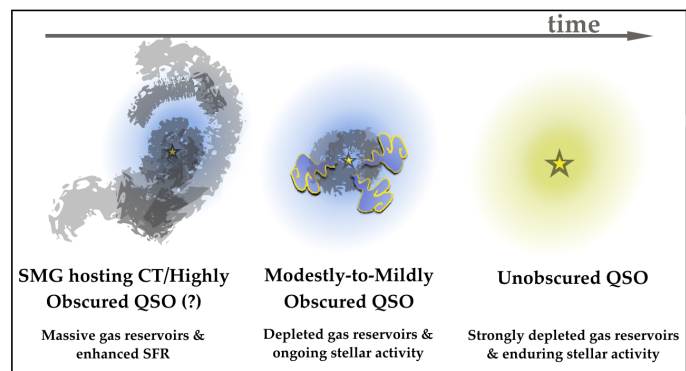


Fig. 1. Schematic diagram to illustrate the standard SB-QSO evolutionary sequence. In the first two panels, the blue ellipse and yellow star represent the galaxy and the central SMBH, respectively; the light and dark grey areas refer to inflowing gas and dust. Dark blue clouds with yellow outlines indicate outflows. In the last panel, the yellow star and ellipse represent the SMBH and the QSO emission. In the first phase (*left*), the central regions are fuelled by huge amounts of gas and dust, and the SMBH is highly obscured. These systems, originating from gas-rich galaxy mergers, are commonly identified as SMGs, and are associated with star formation efficiencies of $\sim 100 \div 200$. The SFE of CT/highly obscured QSOs is mostly unknown. These systems, if tracing the same evolutionary stage, should have SFEs similar to those of SMGs. In the last phase (*right*), the system is revealed as an unobscured QSO (bright enough to easily outshine its host galaxy). In this phase its gas reservoir is expected to be strongly depleted. The SFE measured in optically luminous QSOs can span a wide range, from a few 100 to ~ 2000 . In the transition phase (*middle*), galaxy-wide outflows start to remove the dust and gas reservoirs (which only partially obscure the nuclear regions). We observe these systems as obscured QSOs (generally associated with signatures of outflows). For these systems, we naively expect to observe intermediate SFE between SMGs and unobscured QSOs.

cosmic SF activity and SMBH growth ($z \sim 2$; Cimatti et al. 2006). The identification of distant, buried QSOs is particularly challenging since the high gas column densities absorb their emission below rest frame 10 keV, so that they might be largely missed even in the deepest hard X-ray surveys available today. Because of this limitation, only a few high- z highly obscured ($N_{\text{H}} > 10^{23} \text{ cm}^{-2}$) quasars have been targeted in CO millimetre studies (e.g. Aravena et al. 2008; Coppin et al. 2008, 2010; Polletta et al. 2011).

The purpose of this work is to review our understanding of the molecular gas emission in highly obscured QSO host galaxies. We present the Jansky Very Large Array (JVLA) and the Plateau de Bure Interferometer (PdBI) observations of three obscured QSOs at $z \sim 2$. We also take advantage of the available information for $z > 1$ buried systems in the literature. We test the aforementioned evolutionary scenario, i.e. whether these systems can be considered as the progenitors of optically luminous QSOs, comparing their star formation efficiencies (see Fig. 1). We will also compare the cold gas reservoir of obscured AGN with those of normal MS and SB galaxies with the same stellar mass and redshift to unveil the presence of potential feedback effects.

The paper is organised as follows. In Sect. 2 we present the targets analysed in this work, discussing their properties derived from available multiwavelength information and presenting the PdBI and JVLA observations and data analysis. Section 3 presents the samples of normal and submillimetre galaxies, unobscured and obscured QSOs collected from the literature. In Sect. 4 we show the SFE and gas fractions

¹ In this paper, we use the “empirical” SFE definition, $SFE = L_{\text{IR}}/L'_{\text{CO}}$, rather than the “physical” SFE in units of yr^{-1} . Here L_{IR} refers to the 8–1000 μm integrated stellar infrared luminosity, while L'_{CO} indicates the CO(1-0) luminosity. The advantage of using these empirical measurements is that they are not subject to the uncertainties related to the use of conversion factors needed in the physical formalism for the derivation of gas masses (see Sect. 4.5 in Carilli & Walter 2013).

Table 1. Targets properties.

Target	z	RA (J2000)	Dec (J2000)	$R - K$	MIR/O	$\log(L_X)$ (erg s^{-1})	$\log(N_{\text{H}})$ cm^{-2}	$\log(M_{\text{star}})$ (M_{\odot})	$\log(L_{\text{IR}})$ (L_{\odot})	SFR ($M_{\odot} \text{ yr}^{-1}$)	$\log(\text{sSFR}/\text{sSFR}_{\text{MS}})$	SFE
(1)	(2)	(3)	(4)	(5)	(6)	(7)	(8)	(9)	(10)	(11)	(12)	(13)
BzK4892	2.578 ^{sp}	03:32:35.7	-27:49:16	5.3	2000	43.71 ^{+0.46} _{-0.59}	24.53 ^{+0.32} _{-0.30}	11.26 ± 0.15	12.81 ± 0.01	623 ⁺¹⁵ ₋₂₁	0.23 ± 0.16	>410
BzK8608	2.51 ^{ph}	03:32:20.9	-27:55:46	4.8	300	44.29 ^{+0.09} _{-0.09}	23.75 ^{+0.26} _{-0.20}	10.95 ± 0.10	11.44 ^{+0.34} _{-0.70}	27 ⁺³² ₋₂₅	-0.88 ± 0.57	>11
CDF153	1.536 ^{sp}	03:32:18.3	-27:50:55	5.3	70	44.13 ^{+0.04} _{-0.04}	23.77 ^{+0.12} _{-0.11}	11.11 ± 0.10	11.72 ^{+0.04} _{-0.07}	50 ⁺⁶ ₋₈	-0.43 ± 0.16	>19

Notes. Column (1): galaxy name as reported in the paper. Column (2): spectroscopic redshift from literature for BzK4892 and CDF153; for BzK8608 we reported the photometric redshift derived in this paper. Columns (3) and (4): equatorial coordinates. Columns (5) and (6): $R - K$ colour in Vega system and mid-infrared ($24 \mu\text{m}$) to optical (R band) flux ratio (MIR/O) used to isolate obscured AGN in [Fiore et al. \(2008\)](#). Columns (7) and (8): absorption corrected 2–10 keV X-ray luminosity and column density from [Liu et al. \(2017\)](#). Columns (9) to (12): host galaxy properties derived in this work (Sect. 2). L_{IR} refers to the 8–1000 μm integrated infrared luminosity; the specific star formation rate ratio is obtained as the ratio between the specific star formation rate ($\text{sSFR} = \text{SFR}/M_{\text{star}}$) and that expected for a MS galaxy at given computed stellar mass and redshift (sSFR_{MS}), according to the relation of [Speagle et al. \(2014\)](#). The SFR measurements are obtained from IR luminosities, using the [Kennicutt \(1998\)](#) relation. The quoted uncertainties refer to 1σ confidence levels. Column (13): 3σ upper limit star formation efficiency, in units of $L_{\odot}/(\text{K km s}^{-1} \text{ pc}^2)$.

of the different classes of sources, and discuss these properties in the context of the galaxy evolution paradigm, also taking into account their host galaxy properties. Finally, we summarise our results in the Conclusion Section. A flat universe model with a Hubble constant of $H_0 = 67.7 \text{ km s}^{-1} \text{ Mpc}^{-1}$ and $\Omega_M = 0.307$ ([Planck Collaboration XIII 2016](#)) is adopted. We adopt a Chabrier initial mass function to derive host galaxy properties for the targets presented in this work and for the comparison samples. For the X-ray detected sources reported in this paper, we distinguish between mildly obscured (with $21 \lesssim \log(N_{\text{H}}/\text{cm}^{-2}) < 22$), modestly obscured ($22 \lesssim \log(N_{\text{H}}/\text{cm}^{-2}) < 23$), highly obscured ($23 \lesssim \log(N_{\text{H}}/\text{cm}^{-2}) < 24$) and CT AGN.

2. The targets

The identification and classification of highly obscured and CT AGN are challenging tasks. In fact, X-ray spectroscopic analysis, the most robust method of identifying these systems, is only feasible for a small number of sources because it requires high-quality spectra. These sources have been detected using deep surveys by XMM-Newton (e.g. [Comastri et al. 2011](#); [Lanzuisi et al. 2015](#)), *Chandra* (e.g. [Brightman et al. 2014](#); [Liu et al. 2017](#)), and *Swift* (e.g. [Ricci et al. 2017](#)). The first publications from the NuSTAR survey programs are now further broadening the number of highly obscured sources in the Universe (e.g. [Brightman et al. 2015](#); [Farrah et al. 2016](#); [Marchesi et al. 2018](#); [Masini et al. 2016, 2018](#); [Ursini et al. 2017](#)).

Moreover, given the expected low spatial density of CT AGN in the 2–10 keV band, large area surveys are needed to collect sizeable samples. For this reason, alternative multiwavelength selection techniques based on high-ionisation, narrow optical emission lines ([Vignali et al. 2010](#); [Gilli et al. 2010](#)) or on the ratio between mid-infrared and optical fluxes ([Daddi et al. 2007](#); [Eisenhardt 2012](#); [Fiore et al. 2008, 2009](#)) have been developed in recent years. They seem to represent a promising approach for selecting sizeable samples of highly obscured/CT AGN at $z \sim 1-3$ (see e.g. [Perna et al. 2015b](#); [Picconcelli et al. 2015](#); [Vito et al. 2017](#)). However, they rely on indirect methods, and may still be prone to contamination by less obscured AGN or galaxies (e.g. [Donley et al. 2008](#); see [Brandt & Alexander 2015](#) for a recent review).

The sources analysed in this work were selected from the [Feruglio et al. \(2011, BzK4892 and BzK8608\)](#) and [Comastri et al. \(2011, CDF153\)](#) works on the basis of the presence of high equivalent width FeK emission in the X-ray

($EW \sim 1-2 \text{ keV}$), which constitutes unambiguous evidence for the presence of huge obscuring column densities along the line of sight. This distinguishes them from other samples of obscured AGN that have been studied in the literature, which were selected using multiwavelength selection techniques (e.g. [Banerji et al. 2017](#); [Brusa et al. 2018](#)) or the X-ray hardness ratio (e.g. [Polletta et al. 2011](#)). The properties of the three CO follow-up targets analysed in this work are reported in Table 1.

Our targets have also been observed as part of the 7 Ms *Chandra* Deep Field-South Survey (CDFs; [Liu et al. 2017](#)). The new X-ray spectral analysis² has confirmed the presence of strong iron lines in two out of three sources (BzK4892 and CDF153; see Table 4 in [Liu et al.](#)) and their high obscuration with column density of $N_{\text{H}} \approx 6 \times 10^{23} \text{ cm}^{-2}$ for BzK8608 and CDF153, and of $N_{\text{H}} \approx 3 \times 10^{24} \text{ cm}^{-2}$ for BzK4892. We note that the CT QSO BzK4892 would also be selected by the [Fiore et al. \(2008\)](#) selection criteria as a candidate CT source (see Table 1).

2.1. Host galaxy properties from SED fitting

In order to derive the host galaxy properties of the three targets, we collected the photometric information from the UV to mid-infrared catalogue in the CANDELS/GOODS-S field, published in [Guo et al. \(2013\)](#), and from a new *Herschel* catalogue ([Wang et al. in prep.](#)) which utilises an optimised algorithm for photometry in crowded *Herschel* maps (see Appendix A). ALMA continuum observations at 250 GHz ([Ueda et al. 2018](#)) and 340 GHz ([Elbaz et al. 2018](#)) are also used to better constrain the mm emission of BzK4892. ALMA band 7 observations obtained as part of the programs 2013.1.00884.S (PI: Alexander D.) and 2012.1.00869.S (PI: Mullaney J.R.) are used instead to derive 3σ upper limits on the host galaxy dust emission at 340 GHz for BzK8608 and CDF153, respectively. As the listed uncertainties on broad-band photometry in published catalogues are usually underestimated (i.e. only telescope uncertainties are usually quoted), we increase the nominal uncertainties by a factor of 2 (see also e.g. [Shangguan et al. 2018](#)) in order to take into account systematic errors due to confusion limit or calibrations issues for example (e.g. [Nguyen et al. 2010](#)).

To model the observed spectral energy distribution (SEDs), we adopted the publicly available AGNfitter algorithm ([Calistro Rivera et al. 2016](#)), which implements a Bayesian

² At the time of observations, X-ray properties were derived from the 4 Ms *Chandra* survey (for the BzK sources; [Feruglio et al. 2011](#)) and the ultra-deep ($\approx 3.3 \text{ Ms}$) XMM-Newton survey (CDF153; [Comastri et al. 2011](#)).

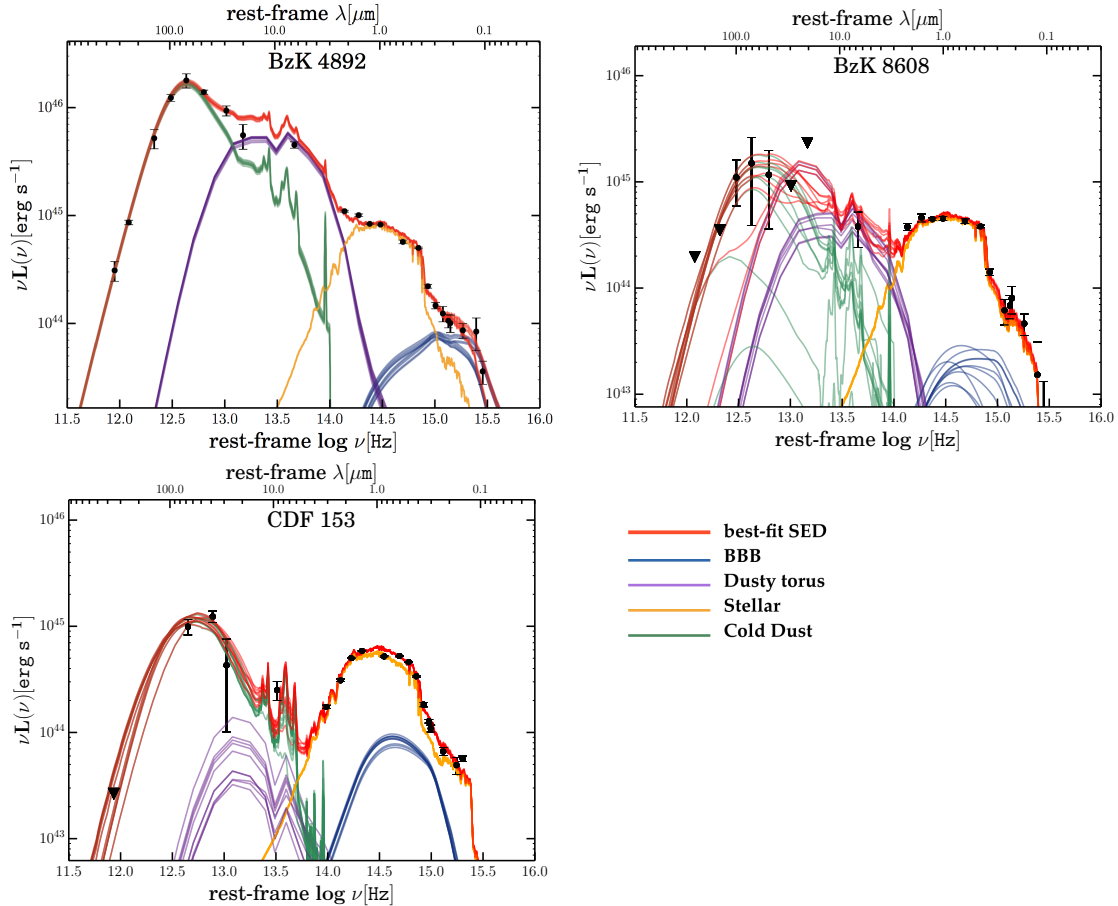


Fig. 2. SED fitting of BzK4892 (*top left panel*), BzK8608 (*top right panel*), and CDF153 (*bottom left panel*). The black dots represent the observed data points from the Guo et al. (2013) and Wang et al. (in prep.) catalogues; 5σ upper limits are shown with black triangles. The data points at $\log(\nu) \sim 12$ are from ALMA continuum observations at 250 GHz and 340 GHz (see Sect. 2). The best-fit SED obtained with AGNfitter (Calistro Rivera et al. 2016) and the different components used to model the SED are shown as labelled in the figure. Ten randomly picked realisations from the posterior distribution function are overplotted in the figures in order to visualise the dynamic range of the parameter values.

Markov chain Monte Carlo (MCMC) method to disentangle the different physical components contributing to the observed SED. The data points have been fitted with a combination of (1) a stellar component, to account for host galaxy contribution; (2) two black hole components, referred to as the “mid-IR torus” and big-blue bump (BBB); and (3) a far-IR to sub-mm emission associated with dust-obscured star formation activity in the host galaxy.

We refer the interested reader to Calistro Rivera et al. (2016) for details on the modelling of the main components described above and the description of the AGNfitter algorithm. Here, we briefly mention that the stellar emission is modelled with stellar population models of Bruzual & Charlot (2003) convolved with exponentially declining star formation histories (SFH), and that stellar templates can be reddened according to the Calzetti et al. (2000) reddening law. The AGN dust emission models are taken from Silva et al. (2004) and consider different templates for unobscured/mildly obscured AGN, modestly obscured, highly obscured and CT AGN. The torus models associated with higher obscurations are characterised by more absorbed near-IR emission and mild silicate absorption at $9.7 \mu\text{m}$ (see Fig. 1 in Calistro Rivera et al. 2016). The BBB emission is modelled using a modified version of the empirical template for type 1 SDSS QSOs constructed by Richards et al. (2006) and considering the possible extinction by applying the SMC reddening law (Prevot 1984) to the BBB template. Both the

reddening values $E(B - V)_{\text{gal}}$ and $E(B - V)_{\text{BBB}}$ range from 0 to 1. Finally, the cold dust emission is modelled using the semi-empirical starburst template libraries by Chary & Elbaz (2001) and Dale & Helou (2002).

Spectroscopic redshifts are available, and are used as input for the SED decomposition with AGNfitter, for BzK4892 and CDF153. They are based on VLT/FORS follow-up (Szokoly et al. 2004). In the case of BzK8608 we adopt a photometric redshift value of $z_{\text{phot}} = 2.51^{+0.16}_{-0.06}$ (Appendix B).

The SED fitting was performed imposing $\log(N_{\text{H}}) > 23$, based on the available information from the X-ray spectroscopic analysis. From the best-fit models shown in Fig. 2, we obtained stellar masses of $\log(M_{\text{star}}/M_{\odot}) \approx 11.0\text{--}11.3$, star formation rates in the range $70\text{--}620 M_{\odot} \text{ yr}^{-1}$, and total (8–1000 μm) stellar infrared luminosities $L_{\text{IR}} \approx (2\text{--}60) \times 10^{11} L_{\odot}$ (see Table 1 for individual measurements).

We note that the BzK4892 SED best fit is clearly reproducing the far-IR and the optical emission from which L_{IR} and M_{star} measurements are derived. The presence of a BBB emission at the bluest wavelengths is instead not well constrained and is responsible for the 0.15 dex uncertainty on the stellar mass estimate. The stellar mass of BzK8608 and CDF153 are instead better constrained (with ~ 0.1 dex uncertainties); on the other hand, their IR luminosities are associated with larger uncertainties (a few ~ 0.1 dex), being these sources much fainter and more affected by blending in the far-IR (Appendix A).

Combining the stellar mass and SFR values derived with AGNfitter, we can compare the specific SFRs ($sSFR = SFR/M_{\text{star}}$) of our targets with typical values of main sequence galaxies. BzK4892 lies slightly above the MS in the $SFR-M_{\text{star}}$ plane at $z \sim 2.5$ (Speagle et al. 2014) and can be classified as a normal MS galaxy (see Table 1; in this work, we classified as starburst all the sources whose $sSFR$ is 0.6 dex above the MS).

High-resolution continuum images at $870 \mu\text{m}$ obtained with ALMA showed that the dust in BzK4892 host galaxy is highly concentrated, i.e. confined inside the galaxy extent seen in the HST rest frame V band (Barro et al. 2016; Elbaz et al. 2018, with a V band effective radius of $\sim 0.5\text{--}0.8 \text{ kpc}$). Coupling the information on the spatial extent observed in the dust continuum image and the SFR inferred from the SED fit, we derive a star formation rate surface density $\Sigma_{\text{SFR}} \sim 140 M_{\odot} \text{ yr}^{-1} \text{ kpc}^{-2}$, similar to those observed in other SMGs (see e.g. Gilli et al. 2014; Yang et al. 2017). Therefore, BzK4892 is plausibly experiencing a very efficient and compact mode of star formation, as expected for merger-driven SB systems (e.g. Hopkins et al. 2006).

BzK8608 and CDF153 have specific star formation rates compatible (within the errors) with the values expected for MS galaxies at their stellar mass and redshift, according to the relation of Speagle et al. (2014), and are therefore associated with MS host galaxies.

2.2. Millimetre observations

BzK4892 and BzK8608 were observed with JVLA (10–12 January 2012), in the DnC configuration, as part of the VLA/11B-060 program (PI: Daddi E.). Observations were carried out with receivers tuned to $\sim 32.5 \text{ GHz}$, corresponding to the expected frequency of the redshifted CO(1-0) emission line, for a total time on source of 4.4 h. An additional window at $\sim 28.3 \text{ GHz}$ was observed in order to attempt a continuum detection in combination with line-free channels in the upper spectral window. Both spectral windows cover a bandwidth of 1 GHz each. We reduced the data with the CASA VLA Calibration pipeline.

CDF153 was observed with PdBI in 2012 with the array set to the C configuration as part of the program W041 (PI. Feruglio C.); the receivers were tuned to the frequency of 91.1 GHz, expected for the CO(2-1) line. The spectral set-up covered a total bandwidth of 2 GHz. The PdBI data were calibrated and imaged with the GILDAS CLIC and MAPPING³ software. The on-source time was 4.8 h (equivalent to six antennas).

The QSO J0329–2357 (for BzK sources) and 0338-214 (CDF153) have been used as phase calibration sources. We used 3C 48 (for BzK sources) and MWC349 (for CDF153) for absolute flux calibrations, which yield an absolute flux accuracy of $\sim 10\%$. The clean beam of the VLA and PdBI observations are reported in Table 2. We note that, due to the low declination of CDF153, the associated PdBI beam is highly elongated.

After flagging poor visibilities, the reduced data sets reached noise levels of $0.04 \text{ mJy beam}^{-1}$ per 40 MHz channel for BzK4892, $0.03 \text{ mJy beam}^{-1}$ per 40 MHz for BzK8608 and $0.29 \text{ mJy beam}^{-1}$ per 120 MHz channels for CDF153 (corresponding to $\approx 400 \text{ km s}^{-1}$, for a “natural” imaging scheme).

These sensitivities were not sufficient to detect the CO line or continuum emission in our targets. However, we were able to infer a stringent 3σ upper limit to the L'_{CO} of $1.6 \times 10^{10} \text{ K km s}^{-1} \text{ pc}^2$ for BzK4892, following Carilli & Walter (2013), and considering typical AGN FWHM_{CO} of 400 km s^{-1} (e.g. Carilli & Walter

Table 2. JVLA and PdBI observations.

Target	Freq. (GHz)	Conf	On-source time (hrs)	FOV (arcsec)	Beam (arcsec)
(1)	(2)	(3)	(4)	(5)	(6)
BzK4892	32.2	DnC	4.4	190×190	2.66×2.35
BzK8608	32.8	DnC	4.2	190×190	2.52×2.10
CDF153	91.1	C	4.8	55×55	24×5

Notes. PdBI observations for CDF153; JVLA observations for BzK targets.

2013; see also Decarli et al. 2018). This upper limit is also consistent with the CO(4-3) luminosity derived from ALMA observations, $L'_{\text{CO}(4-3)} = (1.3 \pm 0.2) \times 10^{10} \text{ K km s}^{-1} \text{ pc}^2$, which will be presented in an upcoming paper (D’Amato et al. in prep.). From the L'_{CO} upper limit we derive a gas fraction $f_{\text{gas}} = M_{\text{gas}}/(M_{\text{star}} + M_{\text{gas}}) < 10\%$, assuming that $M_{\text{gas}} = \alpha_{\text{CO}} L'_{\text{CO}} = 0.8 L'_{\text{CO}}$ (e.g. Bothwell et al. 2013; Carilli & Walter 2013) and that the interstellar medium (ISM) is dominated by molecular gas. We note that the upper limit on the gas fraction we derived from the JVLA observations of the CO(1-0) line is a factor of 4 lower than the values reported by Elbaz et al. (2018) and Barro et al. (2016), derived from dust continuum emission assuming dust-to-gas and mass-metallicity relations (Magdis et al. 2012; Scoville et al. 2016). We suggest that the discrepancy between the different estimates of f_{gas} is due to the large uncertainties still affecting the derivation of gas mass from dust continuum observations. Our CO-based estimate of the molecular gas mass is not dependent on any excitation ratio correction, while the luminosity-to-gas-mass conversion factor $\alpha_{\text{CO}} = 0.8$ was chosen on the basis of the remarkable compactness of the dust continuum emission in the system (Barro et al. 2016; Elbaz et al. 2018). On the other hand, any dust-based estimate of M_{gas} will strongly depend on the assumed metallicity and dust-to-gas ratio.

An alternative interpretation is given by the fact that CO- and dust-based molecular mass measurements can be associated with different timescales: while the CO luminosity is related to the current amount of molecular gas in the host, the production of dust is linked to stellar processes acting over timescales of the order of $\sim 100 \text{ Myr}$ (e.g. Gall et al. 2011). Therefore, the discrepancy between the two estimates can also be explained assuming a rapid decrease in the gas reservoirs in the host galaxy, i.e. assuming recent/ongoing outflow episodes.

For the other two targets, the derived upper limits on the CO(1-0) luminosity are $L'_{\text{CO}} < 2.8 \times 10^{10} \text{ K km s}^{-1} \text{ pc}^2$ for CDF153, assuming a 0.8 excitation correction CO(2-1)/CO(1-0), and $L'_{\text{CO}} < 1.5 \times 10^{10} \text{ K km s}^{-1} \text{ pc}^2$ for BzK8608. Both sources are associated with gas fractions $f_{\text{gas}} \lesssim 50\%$. Despite the presence of an AGN, for these two targets we conservatively assumed $\alpha_{\text{CO}} = 3.6$, the common value adopted for MS galaxies (e.g. Carilli & Walter 2013). The constraints on the gas fractions decrease to $\lesssim 20\%$ if $\alpha_{\text{CO}} = 0.8$ is assumed instead (see e.g. Brusa et al. 2018; Popping et al. 2017 for AGN-hosting MS galaxies with $\alpha_{\text{CO}} < 1$).

We note that for BzK8608, the derived quantities should be considered tentative. Given that no unambiguous spectroscopic redshift has been obtained for this target (see Feruglio et al. 2011; Appendix B), all our measurements were inferred after adopting the photometric redshift derived in Appendix B. We also note that it is possible that the CO(1-0) might fall outside the receiver tuning range, which does not cover the entire 1σ interval associated with our photometric redshift estimate (see Fig. B.1).

³ <http://www.iram.fr/IRAMFR/GILDAS>

3. Literature samples

In order to explore the conditions of molecular gas in high- z galaxies and to test the SB-QSO evolutionary scenario, we combined our new observations with data from the literature, considering different classes of objects at $z > 1$, from normal galaxies and SMGs to obscured and unobscured QSOs. In particular, we consider:

- a sample of 56 main sequence galaxies from the compilation of Sargent et al. (2014), and consisting of sources presented in Daddi et al. (2010), Tacconi et al. (2013), and Magdis et al. (2012);
- a sample of SMGs from Bothwell et al. (2013), Coppin et al. (2008), Silverman et al. (2015), Sharon et al. (2016), Yang et al. (2017), and Yan et al. (2010, see below). For the Bothwell et al. (2013) targets, we distinguished between SMGs with and without AGN. The Coppin et al. (2008) sample consists of ten submillimetre-detected QSOs at $z \sim 2$, for which CO(3-2) or CO(2-1) emission lines have been detected. We also added the dusty highly star-forming galaxies at $z > 4$ collected by Fudamoto et al. (2017), with $\text{SFR} = 2000 \div 8000 M_{\odot} \text{yr}^{-1}$. The final sample of SMGs consists of 66 targets, of which 17 are associated with AGN;
- a sample of unobscured QSOs taken from Carilli & Walter (2013). To these, we added five recently observed targets at $z \sim 6.3$ (three from Venemans et al. 2017 and two from Wang et al. 2013, 2016) and one source at $z \sim 2.5$ from Gullberg et al. (2016). We also added CO-undetected AGN from Evans et al. (1998), Guilloteau et al. (1999), Maiolino et al. (2007), Wang et al. (2011a,b), and one CO-detected target from Solomon & Vanden Bout (2005). The final sample of optically luminous AGN consists of 49 sources.
- a sample of obscured AGN collected from the analyses in the works of Kakkad et al. (2017), Banerji et al. (2017), Fan et al. (2018), and Yan et al. (2010)⁴. We also included further individual targets from Brusa et al. (2018), Polletta et al. (2011), Aravena et al. (2008), Spilker et al. (2016), Stefan et al. (2015), Popping et al. (2017), Vayner et al. (2017) and Emonts et al. (2014), obtaining a final sample of 36 obscured AGN.

In Appendix C we tabulate the information collected separately for each individual class of sources and provide stellar mass and MS-offset ($\text{sSFR}/\text{sSFR}_{\text{MS}}$) distributions for all the sources for which stellar masses are available. These systems are associated with massive host galaxies, with $M_{\text{star}} \approx 10^{11} M_{\odot}$ (with a 1σ dispersion of 0.4 dex). We note that the collected SMGs have been selected in the different papers according to their infrared luminosity $> 10^{12} L_{\odot}$, and that for many of them the M_{star} is unknown; therefore, this sample can include a heterogeneous collection of SB and normal MS galaxies. In the next sections we combine their CO(1-0) luminosities with total IR luminosities and stellar masses to investigate the ISM conditions of the different types of galaxies, also taking into account the presence and the obscuration of accreting SMBHs.

While the ground-state transition CO(1-0) is the preferred emission line for tracing host galaxy molecular gas reservoirs, in many cases we only have access to observations of CO emission lines with $J_{\text{up}} > 1$ (Tables C.1, C.2, C.3). Converting these

to an estimate of the CO(1-0) luminosity requires knowledge of the spectral line energy distribution (SLED), from which it is possible to derive the luminosity ratios between CO states with $J_{\text{up}} > 1$ and the CO(1-0). However, multi-J CO observations reveal a significant diversity of SLED shapes (e.g. Bothwell et al. 2013; Brusa et al. 2018) caused by varying ISM conditions in different systems (e.g. Bothwell et al. 2013); as a result, the conversion to CO(1-0) emission can be highly uncertain when the host galaxy conditions are unknown.

To avoid assumptions for the excitation correction, we used the CO(1-0) measurements reported in Sharon et al. (2016) for the five sources previously observed in $J_{\text{up}} > 1$ CO lines by Coppin et al. (2008) and Bothwell et al. (2013). For all the other objects, the CO(1-0) luminosities used in this work are reported as inferred and tabulated in the different papers, therefore without uniform assumptions about the excitation correction. In fact, as our collected sample is based on different classes of sources, the use of a unique factor would introduce large uncertainties.

Apart from the above-mentioned issues related to the inferred CO(1-0) luminosities, caution is required here also for the (8–1000 μm) infrared luminosities since for most of the collected targets the L_{IR} determination is not self-consistent. Generally, IR luminosity is obtained from SED fitting analysis, distinguishing between AGN and galaxy contributions when complete multiwavelength data are available (e.g. Brusa et al. 2018; Kakkad et al. 2017) or when using a modified greybody model for given temperature and dust emissivity (e.g. Banerji et al. 2017). The reliability of the derived estimates also depends on the availability of (deep) infrared and submillimetre observations of individual targets (see Notes in Table C.2).

Finally, we note that a small fraction of optically luminous QSOs and SMGs are associated with lensed systems (13 SMGs from Yang et al. 2017 and Fudamoto et al. 2017, and 15 QSOs from Carilli & Walter 2013). All lensed galaxy luminosities have therefore been corrected for lens magnification factors, which may be affected by large uncertainties (see e.g. Feruglio et al. 2014; Perna et al. 2018). We are confident, however, that the L_{IR} we report in this work are generally a good approximation of the dust-emission related to SF. In Sect. 4.1.2, we nevertheless discuss what impact systematics errors in L_{IR} measurements could have on our results by *i*) considering only a subsample of sources whose IR luminosities have been derived distinguishing between AGN and galaxy contributions, and *ii*) exploring a scenario where IR luminosity is significantly contaminated by AGN-related emission, in keeping with Duras et al. (2017).

4. Results

4.1. Star formation efficiencies and AGN obscuration

In Fig. 3 (left) we report the CO(1-0) and infrared luminosities for all four classes of targets mentioned above, indicating with star symbols the sources associated with mildly obscured to highly obscured and CT QSOs (the symbols are scaled so that the largest size corresponds to the highest column density; see inset, right panel). To our knowledge, the hyper-luminous galaxies hosting QSOs from (Polletta et al. 2011, SW022550 and SW022513), the SMG/QSO from Coppin et al. (2010, XID403), and the MS galaxy GMASS953 (Popping et al. 2017; Talia et al. 2018) are the only $z > 1$ CT sources for which molecular gas has been studied⁵. The figure highlights the differences between normal galaxies,

⁵ Source C92, from the sample of Kakkad et al. (2017), previously proposed as candidate CT QSO by (Bongiorno 2014, XID 60053), is here associated with a modestly obscured QSO, with $\log(N_{\text{H}}) \sim 22.5 \text{ cm}^{-2}$, on

⁴ The sources MIPS506 and MIPS16144 have been excluded from the sample of obscured AGN on the basis of the presence of strong PAH features in their mid-IR spectra (Yan et al. 2010) and, for MIPS506, the absence of AGN signatures in optical spectra (Bauer et al. 2010). These sources are therefore associated with the SMG sample, as per their $L_{\text{IR}} > 10^{12} L_{\odot}$.

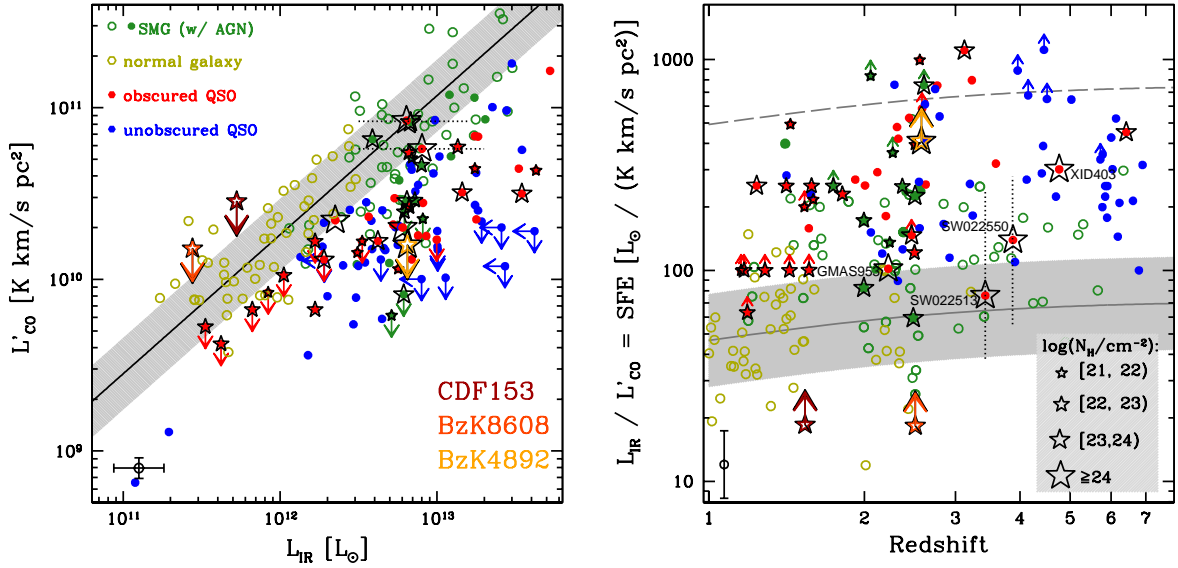


Fig. 3. *Left panel:* observed correlation between measures of CO(1-0) luminosity, L'_{CO} , and (8–1000 μm) IR luminosity, L_{IR} , for the samples of normal galaxies, SMGs, and QSOs at $z > 1$. For the three obscured QSOs described in this paper, we report the 3σ upper limits, as labelled. Open symbols refer to main sequence galaxies and SMG, filled symbols refer to QSOs. Where column density measurements are available, scaled star symbols indicate mild to high N_{H} values, as labelled in the *right panel* inset. Olive green symbols are the galaxies from Sargent et al. (2014); green symbols refer to SMGs from Bothwell et al. (2013), Coppin et al. (2008), and Silverman et al. (2015); red symbols refer to obscured targets. Optically bright QSOs are represented with blue dots. The solid curve represents the best-fit relation derived by (Sargent et al. 2014, 1σ scatter indicated with the grey area), for the MS galaxy sample they collected in the redshift range $0 < z \lesssim 3$. *Right panel:* SFE vs. redshift for the same sample. In this panel, we labelled the names of the four sources from the literature associated with CT QSOs. The solid curve shows the 2-SFM predicted evolutionary trend of MS galaxies of $M_{\text{star}} = 10^{11} M_{\odot}$ (shaded area: illustration of the scatter around the mean evolutionary trend for galaxies with SFR values 1σ above/below the MS). The long-dashed curve is located at 10-fold higher SFE than the mean MS evolutionary trend. Representative 1σ errors on individual data points are shown in the *bottom left* corner of the plots. For the two CT QSOs SW022513 and SW022550, Polletta et al. (2011) indicated a wide range for their IR luminosities (see Notes in Table C.2); these sources are therefore plotted in the *left panel* at the centroid of the IR range, while horizontal dotted lines show the IR luminosity interval. In the right panel we similarly reported the two sources at the centroid positions and indicated the SFE ranges with vertical dotted lines.

which follow the $L_{\text{IR}} - L'_{\text{CO}}$ relation for MS galaxies (solid line, as reported by Sargent et al. 2014), and the obscured QSO population, whose sources are generally below the locus of MS galaxies. In general, optically luminous QSOs are further below the relation. From this plot we note that the majority of SMGs in our sample follow the relation of MS sources.

The three obscured AGN presented in this paper are also shown in the figure. Non-stringent upper limits on the CO luminosities are associated with BzK8608 and CDF153⁶; the upper limit for BzK4892 is instead located well below the $L_{\text{IR}} - L'_{\text{CO}}$ relation for MS galaxies.

In Fig. 3 (right) we show the SFE as a function of redshift for the same compilation of MS galaxies, SMGs, and AGN at $z > 1$. Unobscured AGN show SFE in the range between 100 and 2000, while MS galaxies (SMGs) have $\text{SFE} \lesssim 100$ ($\lesssim 200$). The figure also shows the obscured AGN (red symbols) and the SMGs with AGN activity (filled green symbols), with SFE in the range between ≈ 100 and 1000. The figure shows no clear trend with redshift for the SFE of individual classes of targets; consistent with the slow SFE-evolution at $z > 1$ already discussed in the Introduction.

the basis of deeper *Chandra* observation (Marchesi et al. 2016). Source C1148, from Kakkad et al. (2017), is instead a candidate CT source; however, the target is detected with 20 net counts and deeper observations are required to confirm its high obscuration (Marchesi et al. 2016).
⁶ At the time of observations, the infrared luminosities of BzK8608 and CDF153 were overestimated by a factor of a few (as they were derived on the basis of radio 1.4 GHz observations), and the required depths in CO were settled assuming a SFE = 100.

In particular, it has been observed that the SFE of MS galaxies increases in the redshift range $z \sim 0 - 1$, and then flattens at $z > 1$ (e.g. Sargent et al. 2014; Santini et al. 2014). This trend has been confirmed up to $z \lesssim 3$; at higher redshifts, CO observations of normal MS galaxies are still scarce (e.g. Dessauges-Zavadsky et al. 2017; Magdis et al. 2017), and the SFE evolution is thus primarily constrained by continuum-based gas mass estimates (e.g. Schinnerer et al. 2016) which suggest merely slow evolution also beyond $z \sim 3$. SFE measurements of more luminous star-forming galaxies, i.e. starburst ULIRGs and SMGs (with $L_{\text{IR}} > 10^{12} L_{\odot}$), have instead been derived for large samples of targets both at low- z and in the distant Universe (out to $z \sim 6$) and, similarly to MS galaxies, do not display a strong variation with redshift at $z > 1$ (e.g. Aravena et al. 2016; Feruglio et al. 2014; Magdis et al. 2012; Sargent et al. 2014; Yang et al. 2017). Instead, the SFE evolution of unobscured AGN populations is not well known, with CO follow-up focusing mostly on lensed targets at $z \sim 2-3$ and on very distant ($z > 4$) sources. As unobscured AGN display a wider range of SFE values than MS galaxies and SMGs, the available CO spectroscopy does not reveal any clear trends of SFE with redshift for this class of objects.

In the figure we also show the expected average evolutionary trend of MS galaxies of $M_{\text{star}} = 10^{11} M_{\odot}$ from the 2-SFM (two-star formation mode) framework of Sargent et al. (2014). The 2-SFM was introduced in Sargent et al. (2012), and takes advantage of basic correlated observables (e.g. the MS relation and its evolution with z ; Speagle et al. 2014) to predict the SFE (and molecular gas content; see Sect. 4.2) of MS galaxies at different redshifts. We used a CO-to-gas conversion factor $\alpha_{\text{CO}} = 3.6$ (e.g.

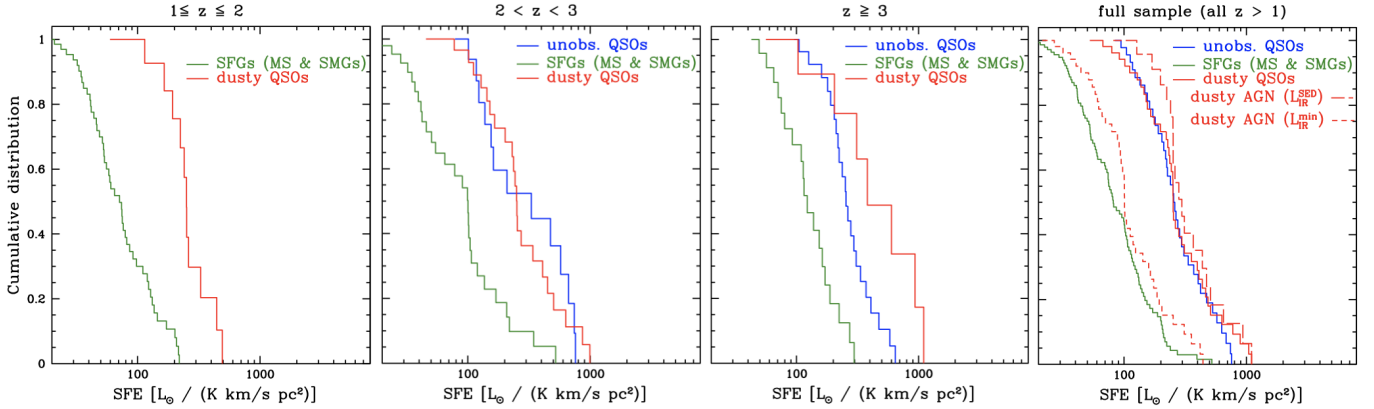


Fig. 4. *First three panels:* cumulative distributions of SFE for the samples of star-forming galaxies (green line), unobscured (blue), and dusty (red) QSOs in the three redshift intervals specified along the upper edge of the figures. All targets collected from the literature (for which SFE measurements can be derived) are used to construct the cumulative distributions; in the first panel, we do not report the cumulative distribution of unobscured AGN (our sample only includes two of these objects at $1 \leq z \leq 2$). The figures show the clear separation in SFE between AGN and SFGs. *Right panel:* cumulative distribution of SFE for the same three samples, considering the entire redshift range covered by our targets. Short-dashed red line: cumulative SFE distribution of dusty AGN obtained by reducing by 60% all their IR luminosities to test for the impact of cool, AGN-heated dust (e.g. [Duras et al. 2017](#); see Sect. 4.1.2 for details). Long-dashed red line: distribution of dusty AGN for which a high-quality L_{IR} has been measured through an SED-decomposition into AGN and galaxy emission.

[Daddi et al. 2010](#)) and the L_{IR} –SFR relation of [Kennicutt \(1998\)](#) to adapt Eq. (22) from [Sargent et al. \(2014\)](#) to our empirical definition of SFE. We also considered the redshift evolution of the MS relation derived by [Speagle et al. \(2014\)](#). The weak 2-SFM trend further emphasises that the redshift evolution of the SFR (and of the SFE) of MS galaxies is not responsible for the heterogeneous distributions shown in Fig. 3 (right) for our different target populations.

On the other hand, values of $\text{SFE} > 100$ can be easily explained by assuming the presence of starburst activity, i.e. considering SFR higher than for MS galaxies (thus enhancing L_{IR}), or by invoking feedback phenomena which depleted the cold gas reservoirs (thus reducing L'_{CO}). As an example, we reported in the figure the predicted trend obtained by assuming a SFR (L'_{CO}) a factor of 10 higher (lower) than a typical MS galaxy.

4.1.1. SFE-contrast between star-forming galaxies and AGN

As already noted by several authors, according to the SB-QSO evolutionary scenario, when an obscured QSO is detected at sub-mm/mm wavelengths, it could be in the transition phase from SMG to an unobscured QSO (e.g. [Coppin et al. 2008](#)). The high SFE values reported in Fig. 3 for these sources are consistent with this scenario. In order to better visualise this result, we report in Fig. 4 the cumulative distributions of SFE for three different subsets of our sample: (1) the MS and submillimetre galaxies without evidence of AGN, combined into a single sample (hereafter “SFG sample”), as MS and SMGs are associated with similar SFE (see Fig. 3); (2) the SMGs with AGN activity (from [Bothwell et al. 2013](#); [Coppin et al. 2008](#)) and the obscured AGN (hereafter referred to as “dusty AGN” for simplicity); and (3) the optically luminous AGN. We also divided the sources into three redshift intervals, $1 < z < 2$, $2 < z < 3$, and $z > 3$, to test the presence of a possible redshift evolution in the properties of AGN targets. The cumulative distributions reported in Fig. 4 highlight the stark differences between star-forming systems and unobscured AGN, with values of $\text{SFE} > 200$ for the large majority ($\sim 80\%$) of luminous AGN and only for a small fraction ($\sim 20\%$) of star-forming galaxies. Instead, the SFE distribution of the population of dusty AGN is similar to that of unobscured AGN.

In order to quantitatively compare the three subsamples, we use the Kolmogorov–Smirnov test (KS test; [Press et al. 1992](#)). The non-parametric KS test measures the probability that two data sets are drawn from the same parent population (“null hypothesis”). The KS statistic for the three redshift intervals is $D \approx 0.6$, which corresponds to a null hypothesis probability rejected at level ~ 90 – 99.8% for the comparisons between the SFE of SFGs and unobscured AGN and also between SFGs and dusty AGN⁷. Overall, the KS tests thus confirm the difference between star-forming systems and AGN. Instead, unobscured and dusty AGN may be associated with the same parent population ($D \approx 0.4$, with a null hypothesis rejected at level $\sim 75\%$), at least at $z > 2$ where we have enough unobscured AGN to perform a statistical test.

The cumulative distributions of the SFGs show a clear evolution with redshift; this can be due to both the slow SFE evolution highlighted in Fig. 3 and to an observational bias (at higher redshifts the sample is dominated by SMGs rather than normal galaxies). The medians of the SFG cumulative distributions evolve from ~ 80 to ~ 130 between the first and last redshift bin shown in Fig. 4. This is the joint effect of the slow SFE evolution of MS galaxies (see Fig. 3 and associated discussion in the text) and an observational bias towards moderately high-SFE starburst SMGs (which represent a higher fraction of our SFG sample relative to MS galaxies at the highest redshifts). Our measurement of the significance of the SFE-gap between the AGN and SFG populations is thus a conservative estimate, as it would widen further if (at the highest redshift) our SFG sample contained similar fractions of MS and SB galaxies as at $z \sim 1$. Dusty and unobscured AGN samples instead suffer from poor statistics and no clear trend can be observed. Given the similar SFE-offsets between AGN and SFGs at all redshifts, we constructed the total cumulative distributions of SFGs, dusty AGN and unobscured AGN in the entire redshift range covered by our literature sample (Fig. 4, right). Also in this

⁷ Lower limit values are not included in the distributions of dusty AGN and unobscured QSOs. The inclusion of these sources, representing $\sim 20\%$ of the samples of dusty AGN and unobscured QSOs, would further increase the SFE-contrast between SFGs and AGN. KS test results are obtained employing the FR/RSS method ([Peterson et al. 1998](#)); the values reported in the text correspond to the average results from 100 iterations.

case, the KS statistic is $D \approx 0.6$ (with a null hypothesis probability rejected at level $\gg 99.9\%$) for the comparisons between the SFE of SFGs and unobscured AGN and also between SFGs and dusty AGN, and $D = 0.25$, with a null hypothesis rejected at level $\sim 75\%$, for the comparison between unobscured and dusty AGN.

The position of the dusty AGN in the SFE cumulative distributions and in the SFE- z plane could suggest that their gas reservoirs have already been affected by feedback. In fact, the systems with low to moderate column densities could be associated with sources in which the feedback processes have already started to clean the line of sight toward the nuclear regions. This argument can be confirmed for the submillimetre-detected AGN in Coppin et al. (2008), for which evidence of ionised outflows have been obtained by the authors from the analysis of near-infrared spectra. Strong, multiphase outflows have also been detected in the obscured QSO at $z = 1.59$, XID2028 (Brusa et al. 2015; Cresci et al. 2015a; Perna et al. 2015a), with SFE ≈ 250 and atypical gas consumption conditions (i.e. very low molecular gas fraction, $f_{\text{gas}} \sim 4\%$; see Brusa et al. 2018).

Figure 3 also shows that two out of the five CT sources in our sample (BzK4892 and XID403) are strongly shifted to low values of CO luminosity (and high SFE). As discussed in the Introduction, however, we would expect such systems to lie on the $L_{\text{IR}} - L'_{\text{CO}}$ relation of MS galaxies (and have SFE $\lesssim 100 - 200$) according to the “classical” SB-QSO evolutionary sequence, where at this stage the molecular gas content should not yet have been affected by feedback according to model predictions (see Fig. 1). Before discussing viable interpretations of these results, we take into account the possible effects of biases in the determination of the SFE values in QSO systems.

4.1.2. Possible biases in SFE derivation for dusty AGN

The empirical SFE = $L_{\text{IR}}/L'_{\text{CO}}$ measurements are a useful instrument for testing the model predictions as they do not depend on the assumption that it is necessary to convert CO luminosity in the molecular gas mass. The SFE is also the best “reference frame” for comparing obscured and unobscured QSOs: comparing gas masses does not provide a meaningful test as they correlate with the mass of the systems which may differ systematically between the two samples; it is also not practical to compare gas fractions as optically luminous QSOs suffer from poorly constrained masses due to AGN-related emission overpowering the light from stars (which also prevents the direct comparison of cold gas properties in mass-matched samples).

On the other hand, the L_{IR} and L'_{CO} measurements (involved in estimating the SFE) are both subject to systematic uncertainties. In particular, CO luminosities may be affected by excitation factor uncertainties (Sect. 4.1). Moreover, the infrared luminosities of our sample have been derived via a variety of approaches and in some cases are poorly constrained due to non-detection in the far-IR bands (see Notes in Table C.2). In this section, we test the impact of these biases on our results, considering the total samples of SFGs, dusty and unobscured AGN (i.e. without considering distinct redshift bins; see Sect. 4.1.1).

In order to probe whether incorrect IR luminosity measurements affect our dusty AGN SFE cumulative distribution, we consider only the subsample of dusty AGN whose L_{IR} has been measured through an SED-decomposition into AGN and galaxy emission. Moreover, we also discarded all AGN for which IR emission is not well constrained because of the lack of data above $24 \mu\text{m}$ (see Notes in Table C.2). The obtained cumulative distribution is shown in Fig. 4, right. A KS test demonstrated that even in this case

the populations of SFGs and dusty AGN are different ($D = 0.57$ and null hypothesis rejected at level $> 99.9\%$).

It has also been suggested that quasar-heated dust on kpc scales can contribute significantly to the far-IR luminosity (e.g. Symeonidis 2017). This contribution, which would not be taken into account with standard SED decomposition involving a mid-IR torus component, can be as high as about 60% for the most luminous sources ($L_{\text{bol}} \sim 10^{48} \text{ erg s}^{-1}$; Duras et al. 2017; see also Symeonidis 2017). In order to test whether the observed difference in the SFE distribution of dusty AGN and star-forming galaxies is due to this bias in L_{IR} measurements, we applied a correction to the SFE values by reducing the IR luminosity by a factor of 60% for all the dusty AGN. We note that this is a very conservative approach: with average absorption-corrected 2–10 keV luminosities of $3 \times 10^{44} \text{ erg s}^{-1}$ (see Table C.2; this corresponds to an average bolometric luminosity of $10^{46} \text{ erg s}^{-1}$, assuming a bolometric correction of 30 following Lusso et al. 2012), our dusty AGN are generally much fainter than the WISSH QSOs presented by Duras et al. (2017) and the sources discussed in Symeonidis (2017).

The distribution derived with rescaled L_{IR} is shown in Fig. 4, right (red dashed line). Even by considering this extreme correction, the SFG and buried AGN cumulative distributions are significantly different (null hypothesis rejected at level $\sim 93\%$; an overlap of the two distributions only becomes possible if we assume that $> 75\%$ of the IR luminosities reported in Table C.2 are associated with quasar emission). We can therefore reasonably exclude that the difference between dusty AGN and SFGs cumulative distributions is due to an overestimation of the AGN host galaxy infrared luminosities.

The excitation factors generally used to derive CO luminosities from $J_{\text{up}} > 1$ states of dusty AGN are 0.8–1.0 (see Notes in Table C.2). We note that smaller values have also been proposed in the literature for the excitation corrections, in particular for high J_{up} states ($J_{\text{up}} > 2$; e.g. Bothwell et al. 2013; Yang et al. 2017; Sharon et al. 2016; up to a factor of 2 smaller); therefore, possible biases in the CO luminosity determination could be responsible for a slight shift to the left in Fig. 4. We therefore consider the SFE distribution of only those sources whose M_{gas} is derived from CO(1-0) and CO(2-1) line fluxes, which are less affected by excitation factor uncertainties, and perform a KS test between the SFGs sample and the subsample of dusty AGN associated with low J transitions. We prove that even in this case the two populations are different ($D = 0.72$; and null hypothesis rejected at level $\gg 99.9\%$).

To summarise, we find no evidence that the observed differences between dusty AGN and star-forming galaxies SFEs are caused by observational biases.

4.2. Low gas fractions in dusty AGN

Figure 5 (left) shows the gas fractions of the 26 dusty AGN for which stellar mass estimates can be derived from multiwavelength data, as a function of redshift. The gas fractions of optically luminous QSOs, instead, are mostly unknown from the observational point of view, and are not reported in the figure⁸.

⁸ The difficulties in deriving unobscured QSO host galaxy stellar masses from SED fitting (see Sect. 4.1.2) make gas fraction estimates for these sources unreliable. An alternative approach is to infer M_{star} via a dynamical mass based on molecular line observations, using the relation $M_{\text{star}} \approx M_{\text{dyn}} - M_{\text{gas}}$ (e.g. Venemans et al. 2017; Wang et al. 2010). However, these measurements are affected by very large uncertainties.

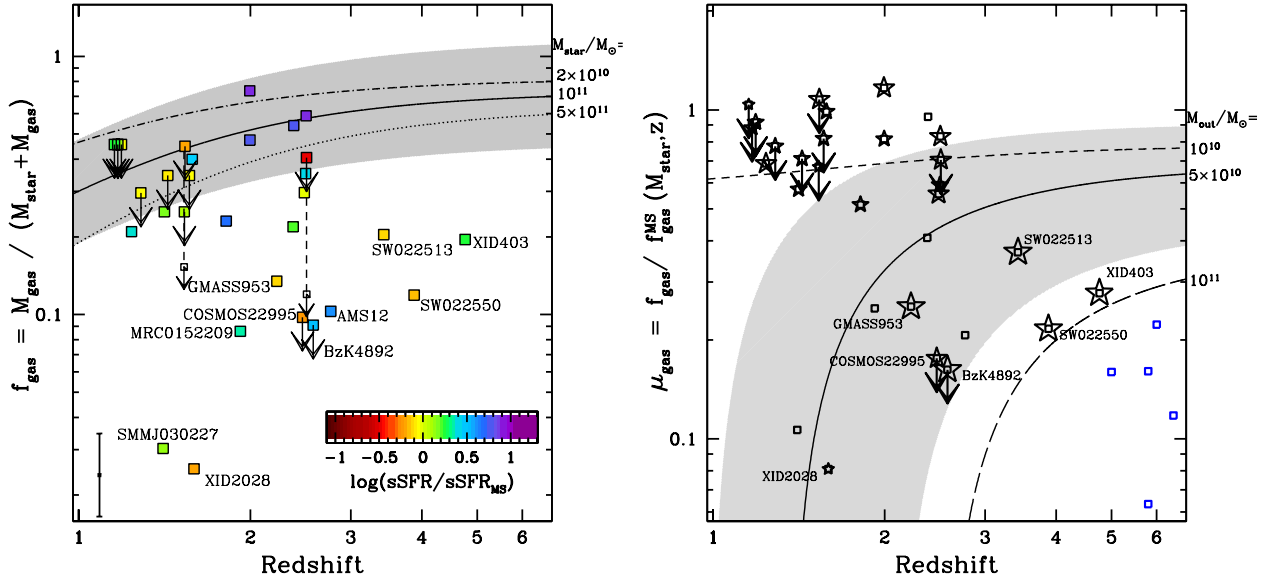


Fig. 5. *Left panel:* redshift evolution of the gas fraction f_{gas} for our sample of dusty AGN. The targets are colour-coded according to the distance from the main sequence of SFGs (see colour bar in the bottom right corner). For BzK8608 and CDF153 we also show (with open symbols) the upper limits we would obtain by assuming $\alpha_{\text{CO}} = 0.8$ instead of 3.6 (see Sect. 2). The predicted evolutionary trend of MS galaxies of $M_{\text{star}} = 10^{11} M_{\odot}$ from the 2-SFM model is shown with a solid curve (shaded area: 1σ scatter around average evolutionary trend line). We also show the predicted trends for MS galaxies of $M_{\text{star}} = 2 \times 10^{10} M_{\odot}$ and $M_{\text{star}} = 5 \times 10^{11}$, as labelled in the figure. The error bar in the bottom left corner of the plot shows the representative 1σ error for the data points (we assume a 0.2 dex uncertainty for M_{star} estimates; see Table C.2). *Right panel:* redshift evolution of the normalised gas fraction μ_{gas} for our sample of dusty AGN. The predicted evolutionary trend of “gas depleted” MS galaxies of $M_{\text{star}} = 10^{11} M_{\odot}$ is shown with the black curve (the shaded area indicates 1σ scatter around the average trend). This trend has been obtained in the framework of the 2-SFM model (Sargent et al. 2014) by considering the depletion of gas due to AGN-driven outflows ($M_{\text{out}} = 5 \times 10^{10} M_{\odot}$). We also display the predicted trends for $M_{\text{out}} = 10^{10}$ and $10^{11} M_{\odot}$. The blue symbols refer instead to the predicted μ_{gas} of high- z unobscured QSOs from Valiante et al. (2014). The star symbols are associated with X-ray detected AGN and are identical to those used in Fig. 3. Essentially all obscured AGN hosts show a gas fraction deficit compared to normal galaxies, with CT QSOs (large star symbols) displaying some of the strongest deficits.

In Fig. 5 we colour-coded the sources according to their distance from the MS (from ~ 1 dex below to $+1.2$ dex above the sequence; see accompanying colour bar). Most galaxies in our SFGs sample and dusty AGN lie on the MS, with the latter population showing slightly higher MS offsets $\text{sSFR}/\text{sSFR}_{\text{MS}}$ (see Fig. C.1).

In the figure the gas fractions are compared with the expected average evolutionary trend of MS galaxies of $M_{\text{star}} = 10^{11} M_{\odot}$ from the 2-SFM framework of Sargent et al. (2014). The 2-SFM trend reproduces well the behaviour of massive ($M_{\text{star}} \approx 10^{10} - 10^{11} M_{\odot}$) MS galaxies (e.g. Schinnerer et al. 2016) and, in this mass range, is also consistent with other gas fraction evolutionary trends in the literature (e.g. Dessauges-Zavadsky et al. 2017; Genzel et al. 2015; Tacconi et al. 2018).

It is still debated whether SBs are expected to have gas fractions that are similar to (e.g. Sargent et al. 2014) or higher than those of MS galaxies (e.g. Genzel et al. 2015; Tacconi et al. 2018). Nevertheless, the 2-SFM trend reproduces well the distribution of the SFGs presented in this work. These targets are not reported in the figure in order not to overpopulate the plot.

Figure 5 (right) also shows that our dusty AGN are preferentially located below the gas fraction relation expected for MS galaxies. Moreover, many of the AGN data points that currently lie on top or above the 2-SFM trend are upper limits. This finding is in line with the idea that dusty AGN are associated with the feedback phase, where the molecular gas content has been depleted by powerful outflows.

Recent cosmological simulations (e.g. Costa et al. 2018) and observations (Brusa et al. 2018; Fiore et al. 2017) both suggest that AGN-driven outflows can have mass outflow rates of the

order of $10^2 - 10^4 M_{\odot} \text{yr}^{-1}$ and that the typical timescales associated with AGN winds are of the order of ~ 10 Myr (e.g. Barai et al. 2018, Costa et al. 2018, Fiore et al. 2017, Hopkins 2005, Hopkins et al. 2016, Perna et al. 2015a and Valiante et al. 2014 for both observational and theoretical arguments). There is also evidence that ejected material is multiphase and predominantly composed of cool gas (e.g. Costa et al. 2018, Zubovas & King 2014; see also Brusa et al. 2018 and Fiore et al. 2017). Cosmological simulations show that the outflow masses can reach $\approx (5 - 80) \times 10^9 M_{\odot}$ during the feedback phase (Costa et al. 2018, and references therein). Interestingly, this estimate is also consistent with observational findings: an outflow mass of $10^{10} M_{\odot}$ can be derived assuming a typical outflow mass rate of $\dot{M}_{\text{out}} \approx 10^3 M_{\odot} \text{yr}^{-1}$ and an outflow timescale of 10 Myr.

We consider all these arguments to derive some predictions for the gas fraction of dusty AGN associated with $M_{\text{star}} = 10^{11} M_{\odot}$ host galaxies. If we assume that dusty AGN are caught 10 Myr after the initial outflow, their gas reservoirs would be depleted by $\approx 5 \times 10^{10} M_{\odot}$; moreover, during this time a given amount of gas is converted into stars, so that $M_{\text{gas}}(t = 10 \text{ Myr}) = M_{\text{gas}}^{\text{MS}} - M_{\text{out}} - \text{SFR} \times \Delta t$, with $M_{\text{gas}}^{\text{MS}}$ from Sargent et al. (2014). Assuming a constant SFR (from the $M_{\text{star}} - \text{SFR}$ relationship), the term $\text{SFR} \times \Delta t$ is negligible with respect to M_{out} . In Fig. 5 (right) we show the predicted trend for “gas depleted galaxies” with the associated 1σ confidence interval. Such a large interval is mostly due to the intrinsic dispersion in the $\text{SFR} - M_{\text{star}}$ MS relation (0.2 dex; Speagle et al. 2014). We also note that at lower redshifts the outflow mass could be overestimated as the cosmological simulations are generally performed at higher redshift ($z \sim 6$), where host galaxies are associated with more rich gas reservoirs (and

the AGN winds can affect larger amounts of gas; see e.g. Fig. 5, left).

In the figure, we also show the normalised gas fractions predicted by Valiante et al. (2014) for optically luminous QSOs at $5 \leq z \leq 6.4$. The authors presented a semi-analytical model for the formation and evolution of high- z QSOs and their host galaxies according to the SB-QSO scenario. They studied the evolution of the stellar and gas masses in order to explain the observed properties of $5 \leq z \leq 6.4$ QSOs. We considered the predicted stellar and gas masses at the end of the evolutionary tracks they presented for five distinct high- z QSOs (Figs. 6 and 7 in Valiante et al.) to derive f_{gas} estimates, and reported in the figure the ratios of these values to the $f_{\text{gas}}^{\text{MS}}(M_{\text{star}}, z)$. Finally, depleted gas reservoirs in $z \sim 6$ galaxies experiencing AGN feedback are also found in the hydrodynamical simulations by Barai et al. (2018), with $f_{\text{gas}} \sim 20\text{--}30\%$ lower with respect to the prelude of the feedback phase (private communication).

An accurate comparison between different predictions and theoretical feedback prescriptions is beyond the purpose of this paper. We refer the reader to (Harrison et al. 2018, and references therein) for a relevant recent review. Here, we simply note that the low gas fractions (and μ_{gas}) we derived for dusty AGN could be explained by recent outflows which depleted their host galaxy cold gas reservoirs.

An alternative interpretation of our results could be that such low μ_{gas} are due to an incorrect estimate of the gas mass because of an incorrect assumption on α_{CO} . In fact, a difference of a factor of 4.5 in M_{gas} easily emerges when we consider $\alpha_{\text{CO}} = 3.6$ instead of 0.8, the value normally used for high- z AGN and SMGs. We note, however, that even assuming $\alpha_{\text{CO}} = 3.6$ for all the sources in our sample (i.e. SFGs and AGN) the population of dusty AGN is still associated with lower μ_{gas} values with respect to SFGs. Moreover, for several dusty AGN the $\alpha_{\text{CO}} = 0.8$ value has been chosen on the basis of the observed compactness and/or temperature of the cold gas reservoirs in the AGN host galaxies (e.g. BzK4892, XID2028, XID403, GMASS953).

We also note that for the few dusty AGN associated with $\alpha_{\text{CO}} = 3.6$ in Fig. 5, i.e. BzK8608, CDF153, and the Kakkad et al. (2017) targets, the CO-to-gas factor has been assumed consistently with other MS galaxies (because of their sSFR), ignoring the presence of the AGN and the possibility that smaller amount of cold gas (by a factor of 4.5) could be present in these systems (Kakkad et al. 2017).

In Fig. 5 (right) we also indicate with variably-sized star symbols the column densities associated with individual AGN (as in Fig. 3). We note that all the sources with lowest μ_{gas} ($f_{\text{gas}} \lesssim 0.2$) are associated with high obscuration ($\log(N_{\text{H}}) \gtrsim 23 \text{ cm}^{-2}$), with the exception of XID2028 ($\log(N_{\text{H}}) \sim 21.84 \text{ cm}^{-2}$)⁹. In particular, all CT QSOs in our sample have strongly depleted molecular gas reservoirs, with $f_{\text{gas}} \lesssim 0.2$ and $\mu_{\text{gas}} \lesssim 0.4$.

We also derived the ratios between the (2–10) keV and IR luminosities per individual target with known absorption-corrected X-ray luminosity. In the framework of a simultaneous evolution between SMBH and host galaxy (Kormendy & Ho 2013), this luminosity ratio can be used to distinguish between SF- and AGN-dominated systems, using as a reference threshold the

⁹ Similar gas fractions are also associated with AMS12, MRC0152-209, and SMMJ030227, for which we do not have X-ray information. HST/ACS observations of the latter target show that this SMG/QSO is a complex system surrounded by a diffuse halo of material in a ring-like structure, with a compact companion at $\sim 1.3''$ ($\sim 11 \text{ kpc}$; Swinbank et al. 2006). Spectroscopic observations of this peculiar target also suggest the presence of complex kinematics between the nuclei (Harrison et al. 2012; Menéndez-Delmestre et al. 2013).

ratio $\log(L_{\text{X}}/L_{\text{IR}}) = -2.2$ (see Sect. 4.4 in Ueda et al. 2018). We found that all but a few sources in our sample are associated with dominant AGN activity (i.e. $\log(L_{\text{X}}/L_{\text{IR}}) > -2.2$) and that there is no obvious correlation between μ_{gas} and $L_{\text{X}}/L_{\text{IR}}$. The high fraction of AGN-dominated starbursting systems in the sample can be plausibly due to observational bias: the multiwavelength information required to recover stellar masses, and infrared and X-ray luminosities could be, in fact, only available for the most extreme sources at $z > 1$.

In summary, we conclude that the gas fraction of dusty AGN and of CT systems in particular strongly differ from MS and SB galaxies without evidence of AGN activity.

4.3. SB-QSO evolutionary sequence vs. orientation-based unification scheme

It has been proposed that gas-rich galaxy major mergers funnel a significant amount of matter toward the nuclear regions, triggering SMBH and starburst activity. Evidence supporting a merger-driven scenario has recently been proposed by Fan et al. (2018), who report CO line emission from a hyper-luminous, dust-obscured QSO at $z \gtrsim 3$ suggesting the presence of gas-rich major mergers in the system (see also Polletta et al. 2011). Gas-rich mergers related to high- z SMG/QSOs have also been recently presented by Trakhtenbrot et al. (2017) and Fogasy et al. (2017, see also Banerji et al. 2017; Vignali et al. 2018). In the SB-QSO framework, these systems would be associated with the initial evolutionary stages before feedback phenomena start to deplete the cold gas.

Moreover, massive, powerful multiphase outflows have been discovered in several local (Feruglio et al. 2010; Perna et al. 2017; Sturm 2011; Veilleux et al. 2017) and high-redshift galaxies hosting obscured AGN (Brusa et al. 2018; Cresci et al. 2015a; Fan et al. 2018; Feruglio et al. 2017; Nesvadba et al. 2016; Popping et al. 2017), demonstrating that luminous AGN are capable of expelling large amounts of gas from the host galaxies, thereby potentially explaining the low gas fraction (and high SFE) of optically luminous QSOs. We note, however, that from an observational point of view, there is not a clear separation between the two classes of dusty AGN: the first is associated with the prelude of the feedback phase (and therefore with more massive gas reservoirs and higher obscuration) and the second is associated with the feedback stage (and moderate column densities). This is the reason why CO-follow up of CT AGN, more reasonably associated with the prelude of the blow-out phase, are essential in order to test the SB-QSO scenario.

We find that the molecular gas reservoirs of dusty AGN are significantly different from those of SFGs (i.e. MS and submillimetre galaxies without evidence of AGN): Figs. 3 and 4 show that SFE in the dusty AGN sample are higher than those of SFGs. This difference cannot be removed considering the biases in CO and infrared luminosity determinations. In Fig. 5 we also show that the gas fraction of dusty AGN is generally lower than that expected for MS and SB galaxies. However, the SFEs of dusty AGN and unobscured QSOs are similar (and clearly higher than those of SFGs), counter to what we would naively expect for sources in a transition phase between SBs and optically bright QSOs. This result could suggest that the similarly enhanced SFEs in optically bright and dusty AGN do not imply a temporal sequence, but that similar mechanisms are in act in these systems.

Considering only the CT QSOs, we find that two out of the five observed systems (i.e. BzK4892 and XID403) are associated with high SFE ($\gtrsim 300$). This finding is also at odds with the SB-QSO evolutionary paradigm, as we would expect that the star formation

efficiency of CT sources should be more similar to that of starburst galaxies (i.e. $\lesssim 200$; see Fig. 4). Moreover, all the CT AGN in our sample have $\mu_{\text{gas}} \lesssim 0.4$ (Fig. 5, right).

One possible explanation for the high SFE values and low gas fractions in CT sources is that these powerful dusty AGN might be already able to quickly clear the gas from the host disk through feedback in this early stage. This hypothesis is confirmed by the presence of strong ionised outflows in the other CT QSOs in our sample, SW022550 and SW022513 (Polletta et al. 2011), for which deep spectroscopic information have been used to study the gas kinematics in the host galaxies, and GMASS953, for which there are several indications of the presence of AGN-driven large-scale outflows (Talia et al. 2018; see also Perna et al. 2015b for another example of powerful outflow in a CT QSO at high- z). We note, however, that these three CT AGN are also associated with lower SFEs with respect to XID403 and BzK4892 and, therefore, that more extreme conditions might be present in the latter AGN (e.g. the concomitant presence of strong SF and AGN activity).

An alternative scenario is given by the possible presence of positive feedback in the host galaxies: AGN could in fact enhance the SF by outflow-induced pressure (e.g. Cresci et al. 2015a,b; Cresci & Maiolino 2018; Silk 2013; see also Maiolino et al. 2017). In this case, the high SFR observed in the host galaxy may be associated with residual star formation activity in an already gas depleted host galaxy. The available information does not allow us to discriminate between positive and negative feedback scenarios; with deep, spatially resolved CO spectroscopy it would be possible to map the molecular gas reservoirs and study the effects of outflows (e.g. Brusa et al. 2018; Carniani et al. 2017).

Finally, it is worth noting that our results could be discussed in the context of the unified model (Antonucci 1993). According to the orientation-based unification scheme, orientation effects relative to an obscuring medium which hides the view of the inner SMBH are responsible for the differences between obscured (type 2) and unobscured (type 1) QSOs¹⁰. Therefore, these systems should be associated, on average, with similar host galaxy properties (i.e. molecular gas content and infrared luminosities). There is evidence suggesting that obscured quasars have higher average SFR and infrared luminosities than the unobscured systems (e.g. Chen et al. 2015; Hiner et al. 2009; Zakamska et al. 2016). Given this observed diversity in IR luminosity and assuming that both QSO classes have similar molecular gas reservoirs, we should observe the highest SFE in dusty systems, in contradiction with our results. This could be interpreted as evidence that the unified model cannot explain the observed SFE of high- z QSOs.

Further investigation is required, however, to probe the absence of biases in actual observations, in particular to discriminate between galaxy-scale absorbers and the presence of a torus in dusty AGN, although gas rich-galaxies could be preferentially selected within type 2 AGN samples (see e.g. the discussion in Zakamska et al. 2016). Under the assumption that cold gas is isotropically distributed in the host, we also note that the high column densities observed in all CT QSOs but SW022513 (for which we do not have information regarding CO extension) can be accounted for by the presence of cold gas on a kp scale rather than, or in addition to, the nuclear (pc-scale) torus (see Gilli et al. 2014 for details). A further caveat is the small number of CT sources

with available CO spectroscopy. In the future, a larger sample of this class of sources will be helpful in confirming our results.

5. Conclusions

We presented JVLA and PdBI observations for two highly obscured (BzK8608 and CDF153) and one Compton-thick (BzK4892) QSOs. We targeted the CO(1-0) line in BzK4892 and BzK8608, both at redshift $z \sim 2.5$, and the CO(2-1) transition in CDF153, at redshift $z = 1.536$. These observations allowed us to place upper limits on the strength of the CO emission lines, corresponding to $L'_{\text{CO}} < (1.5-2.8) \times 10^{10} \text{ K km s}^{-1} \text{ pc}^2$ for the three targets. We used AGNfitter (Calistro Rivera et al. 2016) to fit their SEDs and decompose AGN and galaxy emission, obtaining estimates of the infrared luminosity and the stellar mass of the host galaxies.

When we place these targets in the $L'_{\text{CO}} - L_{\text{IR}}$ plane (Fig. 3) and compare their positions with respect to the relation expected for MS galaxies, we find that BzK4892 is the only target for which we were able to derive a physically stringent upper limit on the CO luminosity. This source displays a high star formation rate surface density, $\Sigma_{\text{SFR}} \sim 130 M_{\odot} \text{ yr}^{-1} \text{ kpc}^{-2}$ (for an effective radius $r_e = 0.8 \text{ kpc}$; Barro et al. 2016), a low gas fraction ($f_{\text{gas}} < 0.06$), and a star formation efficiency SFE > 410 , pointing to an advanced level of gas depletion in this CT QSO. Instead, for BzK8608 and CDF153 the derived upper limits on the gas fractions ($f_{\text{gas}} \lesssim 0.5$) and lower limits on the SFE of ≈ 20 are compatible with available measurements for normal MS and SMGs. Lower gas fractions would be inferred from our CO observations if these sources can be shown to have ISM conditions generally associated with low CO-to-gas conversion factors (e.g. high Σ_{SFR} and/or high T_{dust}). We also reiterate here that for BzK8608, all measurements should be regarded as tentative measurements because of the adopted photometric redshift (Sect. 2.2).

In the second part of the paper, we combined our measurements with a sample comprising normal and submillimetre galaxies, plus dusty (see Sect. 4.1.2) and unobscured AGN at $z > 1$ from the literature. Our results suggest that submillimetre detected, dusty AGN are associated with star formation efficiencies very similar to those of unobscured QSOs, and higher than those of SFGs.

Furthermore, we found that CT QSOs may behave more similarly to optically luminous QSOs and obscured AGN than to SMGs: indication of outflows in the ionised and molecular phases of the ISM (SW022550, SW022513, and GMASS953) and indirect evidence of depleted gas (BzK4892) point to the possibility that, in the context of the SB-QSO paradigm, highly obscured systems are affected by feedback phenomena right from the early phases of the evolutionary sequence. We would like to note that evidence of outflows even in early- or intermediate-stage merger systems has been collected for several nearby ULIRG/AGN galaxies (e.g. Feruglio et al. 2013, 2015; Rupke & Veilleux 2013, 2015; Saito et al. 2018) and in the 3C 298 radio-loud QSO at $z = 1.439$ (Vayner et al. 2017; see also Sect. 4.3; footnote 9). These results, together with the fact that SFE of dusty and unobscured QSOs are comparable on average, could be consistent with the SB-QSO evolutionary scenario assuming that feedback effects occur early in the evolutionary sequence.

Our findings are not in tension with recent observational and theoretical work showing that the SFR of galaxies hosting AGN is not strongly affected by feedback (e.g. Mullaney et al. 2015; Roos et al. 2015): the high SFE in our dusty AGN is reasonably due to depleted cold gas reservoirs (see Fig. 5) rather than

¹⁰ AGN with discordant optical (type1/type2) and X-ray (unobscured/obscured) classification have been reported in the literature. In this work we do not take into account this discrepancy since these sources represent a small fraction of the AGN population (see e.g. Merloni et al. 2014; Ordovás-Pascual et al. 2017 for details).

significant SFR variations. We also note that, with respect to the Mullaney et al. (2015) sample mostly comprising MS galaxies hosting AGN, in this paper we consider starbursting, dusty AGN, which are expected to be affected by strong outflows (e.g. Hopkins et al. 2008).

We also want to emphasise that particular chemical and kinematic conditions could be at the origin of the observed $L_{\text{IR}}/L'_{\text{CO}}$ ratios (e.g. Blitz & Rosolowsky 2006; Saintonge et al. 2016; Shi et al. 2011), and the similarly enhanced SFE (and depleted gas reservoirs) in optically bright and dusty AGN could not necessarily imply a temporal sequence for the two samples. For example, powerful outflows, revealed both in highly obscured and optically bright QSOs (e.g. Bischetti et al. 2016; Carniani et al. 2017; Perna et al. 2015b), could peculiarly alter the cold gas conditions and be responsible for the enhanced SFE values. The exact interpretation of our results needs further exploration.

We also emphasise that the small number of highly obscured sources and the uncertainties still affecting the measurements of both CO and IR luminosities do not allow us to draw any strong conclusion about the physical conditions in these distant buried QSOs and the possible evolutionary connection between unobscured and highly obscured AGN. Further observations of high- z SMG/QSOs with the JVLA, ALMA, and/or NOEMA facilities will help shed light on the exact nature of the host galaxies of rapidly growing SMBHs, both in terms of assembling larger samples, and also of obtaining higher spatial resolution detections to determine the direct effects of feedback phenomena on the host galaxy gas reservoirs.

Finally, we also want to emphasise that CO(1-0) measurements in high- z galaxies are of enormous utility to the study of galaxy evolution as they are not affected by excitation correction uncertainties and can be used to compare galaxies with unknown and possibly different physical conditions. The CO(1-0) luminosity can be used to derive molecular gas content in the host galaxy, assuming a luminosity-to-gas-mass conversion factor. This estimate is arguably less affected by the uncertainties than measurements based on dust continuum observations, for which assumptions on the dust-to-gas ratios and/or metallicity and dust temperature are required (e.g. Magdis et al. 2012; Scoville et al. 2016). Existing CO(1-0) observations, however, have so far been limited to a small number of sources (see e.g. Table C.2 for the sample of dusty AGN); the measurements reported in this paper for BzK4892 would therefore be useful for establishing the context for the next studies of highly obscured QSOs in the high- z Universe.

Acknowledgements. We thank the anonymous referee for a useful and detailed report which helped improve the paper. MP thanks the Marco Polo Project of Bologna University and the University of Sussex for the hospitality during his stay in Brighton, where part of this work was carried out. MP also thanks S. Salvadori, S. Gallerani, A. Pallottini, M. C. Orofino, and L. Graziani for fruitful discussions. GC acknowledges the support by INAF/Frontiera through the “Progetti Premiali” funding scheme of the Italian Ministry of Education, University, and Research, and the INAF PRIN-SKA 2017 programme 1.05.01.88.04. Much of this research was carried out at the Munich Institute for Astro- and Particle Physics (MIAPP) of the DFG cluster of excellence “Origin and Structure of the Universe” during the program “In & Out: What rules the galaxy baryon cycle?” (July 2017). MP, MB, and GL acknowledge support from the FP7 Career Integration Grant “eEASy” (“SMBH evolution through cosmic time: from current surveys to eROSITA-Euclid AGN Synergies”, CIG 321913). MTS was supported by a Royal Society Leverhulme Trust Senior Research Fellowship (LT150041). EL is supported by a European Union COFUND/Durham Junior Research Fellowship (under EU grant agreement no. 609412). This work is based on observations carried out under project number W041 [PI: C. Feruglio], with the IRAM PdBI Interferometer [30m telescope], and under project number VLA/11B-060 [PI: E. Daddi], with the JVLA telescope. IRAM is supported by INSU/CNRS

(France), MPG (Germany), and IGN (Spain). The National Radio Astronomy Observatory is a facility of the National Science Foundation operated under cooperative agreement by Associated Universities, Inc. This work has made use of the Rainbow Cosmological Surveys Database, which is operated by the Universidad Complutense de Madrid (UCM), partnered with the University of California Observatories at Santa Cruz (UCO/Lick, UCSC).

References

- Alexander, D. M., Smail, I., Bauer, F. E., et al. 2005, *Nature*, 434, 738
 Anguita, T., Faure, C., Yonehara, A., et al. 2008, *A&A*, 481, 615
 Antonucci, R. 1993, *ARA&A*, 31, 473
 Aravena, M., Bertoldi, F., Schinnerer, E., et al. 2008, *A&A*, 491, 173
 Aravena, M., Hodge, J. A., Wagg, J., et al. 2014, *MNRAS*, 442, 558
 Aravena, M., Spilker, J. S., Bethermin, M., et al. 2016, *MNRAS*, 457, 4406
 Bañados, E., Venemans, B. P., Decarli, R., et al. 2016, *ApJS*, 227, 11
 Banerji, M., Fabian, A. C., & McMahon, R. G. 2014, *MNRAS*, 439, L51
 Banerji, M., Carilli, C. L., Jones, G., et al. 2017, *MNRAS*, 465, 4390
 Barai, P., Gallerani, S., & Pallottini, A. 2018, *MNRAS*, 473, 4003
 Barro, G., Kriek, M., Pérez-González, P. G., et al. 2016, *ApJ*, 827, 32
 Bauer, F. R., Yan, L., Sajina, A., et al. 2010, *ApJ*, 710, 212
 Bischetti, M., Piconcelli, E., Vietri, G., et al. 2016, *A&A*, 598, A122
 Blitz, L., & Rosolowsky, E. 2006, *ApJ*, 650, 933
 Bongiorno, A., Maiolino R., Brusa, M., et al. 2014, *MNRAS*, 443, 2077
 Bothwell, M. S., Smail, I., Chapman, S. C., et al. 2013, *MNRAS*, 429, 3047
 Brandt, W. N., & Alexander, D. M. 2015, *A&ARv*, 23, 1
 Brightman, M., Nandra, K., Salvato, M., et al. 2014, *MNRAS*, 443, 1999
 Brightman, M., Baloković, M., Stern, D., et al. 2015, *ApJ*, 805, 41
 Brusa, M., Bongiorno, A., Cresci, G., et al. 2015, *MNRAS*, 446, 2394
 Brusa, M., Perna, M., Cresci, G., et al. 2016, *A&A*, 588, A58
 Brusa, M., Cresci, G., Daddi, E., et al. 2018, *A&A*, 612, A29
 Bruzual, G., & Charlot, S. 2003, *MNRAS*, 344, 1000
 Buchner, J., Georgakakis, A., Nandra, K., et al. 2014, *A&A*, 564, A125
 Calistro Rivera, G., Lusso, E., Hennawi, J. F., & Hogg, D. W. 2016, *ApJ*, 833, 98
 Calzetti, D., Armus, L., Bohlin, R. C., et al. 2000, *ApJ*, 533, 682
 Carilli, C. L., & Walter, F. 2013, *ARA&A*, 51, 105
 Carniani, S., Marconi, A., Maiolino, R., et al. 2017, *A&A*, 605, A105
 Cimatti, A., Daddi, A., & Renzini, A. 2006, *A&A*, 453, L29
 Chary, R., & Elbaz, D. 2001, *ApJ*, 556, 562
 Chen, C. J., Hickox, R. C., Alberts, S., et al. 2015, *ApJ*, 802, 102
 Comastri, A., Ranalli, P., Iwasawa, K., et al. 2011, *A&A*, 526, L9
 Coppin, K. E. K., Swinbank, A. M., Neri, R., et al. 2008, *MNRAS*, 389, 45
 Coppin, K. E. K., Chapman, S. C., Smail, I., et al. 2010, *MNRAS*, 407, L103
 Costa, T., Rosdahl, J., Sijacki, D., & Haehnelt, M. G. 2018, *MNRAS*, 479, 2079
 Cresci, G., & Maiolino, R. 2018, *NatAs*, 2, 179
 Cresci, G., Mainieri, V., Brusa, M., et al. 2015a, *ApJ*, 799, 81
 Cresci, G., Marconi, A., Zibetti, S., et al. 2015b, *A&A*, 582, A63
 D’Agostini, G. 2003, *Bayesian Reasoning in Data Analysis: A Critical Introduction*, *J. Am. Stat. Ass.*
 Daddi, E., Alexander, D. M., Dickinson, M., et al. 2007, *ApJ*, 670, 173
 Daddi, E., Elbaz, D., Walter, F., et al. 2010, *ApJ*, 714, 118
 Dale, D. A., & Helou, G. 2002, *ApJ*, 576, 159
 Decarli, R., Walter, F., Venemans, B. P., et al. 2018, *ApJ*, 854, 97
 Dessauges-Zavadsky, M., Zamojski, M., Rujopakarn, W., et al. 2017, *A&A*, 605, A81
 Di Matteo, T., Springel, V., & Hernquist, L. 2005, *Nature*, 433, 604
 Di Matteo, T., Combes, F., Mechior, A. L., & Semelin, B. 2007, *A&A*, 468, 61
 Donley, J. L., Rieke, G. H., Pérez-González, P. G., & Barro, G. 2008, *ApJ*, 687, 111
 Duras, F., Bongiorno, A., Piconcelli, E., et al. 2017, *A&A*, 604, A67
 Eisenhardt, P. R. M., Wu, J., Tsai, C.-W., et al. 2012, *ApJ*, 755, 173
 Elbaz, D., Dickinson, M., Hwang, H. S., et al. 2011, *A&A*, 533, A119
 Elbaz, D., Leiton, R., & Nagar, N., et al. 2018, *A&A*, 616, A110
 Elvis, M., Hao, H., Civano, F., et al. 2012, *ApJ*, 759, 6
 Emonts, B. H. C., Norris, R. P., & Feain, I. 2014, *MNRAS*, 438, 2898
 Evans, A. S., Sanders, D. B., Cutri, R. M., et al. 1998, *ApJ*, 506, 205
 Fan, L., Knudsen, K. K., Fogasy, J., & Drouart, G. 2018, *ApJ*, 856, 5
 Farrar, D., Baloković, M., Stern, D., et al. 2016, *ApJ*, 831, 76
 Feruglio, C., Maiolino, R., Piconcelli, E., et al. 2010, *A&A*, 518, L155
 Feruglio, C., Daddi, E., Fiore, F., et al. 2011, *ApJ*, 729, L4
 Feruglio, C., Fiore, F., Piconcelli, E., et al. 2013, *A&A*, 558, A87
 Feruglio, C., Bongiorno, A., Fiore, F., et al. 2014, *A&A*, 565, A91
 Feruglio, C., Fiore, F., Carniani, S., et al. 2015, *A&A*, 583, A99
 Feruglio, C., Ferrara, A., Bischetti, M., et al. 2017, *A&A*, 608, A30
 Fiore, F., Grazian, A., Santini, P., et al. 2008, *ApJ*, 672, 94
 Fiore, F., Puccetti, S., Brusa, M., et al. 2009, *ApJ*, 693, 447

- Fiore, F., Feruglio, C., Shankar, F., et al. 2017, *A&A*, 601, A143
- Fogasy, J., Knudsen, K. K., Lagos, C. D. P., et al. 2017, *A&A*, 597, A123
- Fudamoto, Y., Ivison, R. J., Oteo, I., et al. 2017, *MNRAS*, 472, 2028
- Gall, C., Andersen, A. C., & Hjorth, J. 2011, *A&A*, 528, A14
- Gallerani, S., Zappacosta, L., Orofino, M. C., et al. 2017, *MNRAS*, 467, 3590
- Genzel, R., Tacconi, L. J., Lutz, D., et al. 2015, *ApJ*, 800, 20
- Gilli, R., Vignali, C., Mignoli, M., et al. 2010, *A&A*, 519, A92
- Gilli, R., Su, J., Norman, C., et al. 2011, *ApJ*, 730, 28
- Gilli, R., Norman, C., Vignali, C., et al. 2014, *A&A*, 562, A67
- Guilloteau, S., Omont, A., Cox, P., et al. 1999, *A&A*, 349, 363
- Gullberg, B., De Breuck, C., Lehnert, M. D., et al. 2016, *A&A*, 586, A124
- Guo, Y., Ferguson, H. C., Giavalisco, M., et al. 2013, *ApJS*, 207, 24
- Harrison, C. M., Alexander, D. M., Swinbank, A. M., et al. 2012, *MNRAS*, 426, 1073
- Harrison, C. M., Costa, T., Tadhunter, C. N., et al. 2018, *NatAs*, 2, 198
- Hiner, K. D., Canalizo, G., Lacy, M., et al. 2009, *ApJ*, 706, 508
- Hopkins, P. F. 2012, *MNRAS*, 420, 8
- Hopkins, P. F., Hernquist, L., Martini, P., et al. 2005, *ApJ*, 625, L71
- Hopkins, P. F., Hernquist, L., Cox, T. J., et al. 2006, *ApJS*, 163, 1
- Hopkins, P. F., Hernquist, L., Cox, T. J., & Keres, D. 2008, *ApJS*, 175, 356
- Hopkins, P. F., Torrey, P., Faucher-Giguere, C., et al. 2016, *MNRAS*, 458, 816
- Hsu, L., Salvato, M., Nandra, K., et al. 2014, *ApJ*, 796, 60
- Isaak, K. G., Priddey, R. S., McMahon, R. G., et al. 2002, *MNRAS*, 329, 149
- Jahnke, K., & Macciò, A. V. 2011, *ApJ*, 734, 92
- Kormendy, J., & Ho, L. C. 2013, *ARA&A*, 51, 511
- Kakkad, D., Mainieri, V., Brusa, M., et al. 2017, *MNRAS*, 468, 4205
- Kennicutt, R. C. 1998, *ARA&A*, 36, 189
- Kennicutt, R. C., & Evans, N. J. 2012, *ARA&A*, 50, 513
- Laird, E. A., Nandra, K., & Pope, A. 2010, *MNRAS*, 401, 2763
- Lanzuisi, G., Ranalli, P., Georgantopoulos, I., et al. 2015, *A&A*, 573, A137
- Lanzuisi, G., Delvecchio, I., Berta, S., et al. 2017, *A&A*, 602, A123
- Leipski, C., Meisenheimer, K., Walter, F., et al. 2013, *ApJ*, 772, 103
- Leroy, A. K., Walter, F., Brinks, E., et al. 2008, *AJ*, 137, 2782
- Liu, T., Tozzi, P., & Wang, J. X. et al. 2017, *ApJS*, 232, 8
- Luo, B., Brandt, W. N., Xue, Y. Q., et al. 2017, *ApJS*, 228, 2
- Lusso, E., Comastri, A., Simmons, B. D., et al. 2012, *MNRAS*, 425, 623
- Lyu, J., Rieke, G. H., & Alberts, S. 2016, *ApJ*, 816, 85
- Martínez-Sansigre, A., Karim, A., Schinnerer, E., et al. 2009, *ApJ*, 706, 184
- Magdis, G. E., Daddi, E., Sargent, M., et al. 2012, *ApJ*, 760, 6
- Magdis, G. E., Rigopoulos, D., Daddi, E., et al. 2017, *A&A*, 603, A93
- Magnelli, B., Popesso, P., Berta, S., et al. 2013, *A&A*, 553, A132
- Maiolino, R., Shemmer, O., Imanishi, M., et al. 2007, *A&A*, 472, 33
- Maiolino, R., Gallerani, S., Neri, R., et al. 2012, *MNRAS*, 425, L66
- Maiolino, R., Russell, H. R., Fabian, A. C., et al. 2017, *Nature*, 544, 202
- Manners, J. C., Johnson, O., Almaini, O., et al. 2003, *MNRAS*, 343, 293
- Marchesi, S., Lanzuisi, G., Civano, F., et al. 2016, *ApJ*, 830, 100
- Marchesi, S., Ajello, M., Marcotulli, L., et al. 2018, *ApJ*, 854, 49
- Martocchia, S., Piconcelli, E., Zappacosta, L., et al. 2017, *A&A*, 608, A51
- Masini, A., Comastri, A., Baloković, M., et al. 2016, *A&A*, 589, A59
- Masini, A., Civano, F., Comastri, A., et al. 2018, *ApJS*, 235, 17
- Mazzucchelli, C., Bañados, C., Venemans, B. P., et al. 2017, *ApJ*, 849, 91
- Menci, N., Fiore, F., Puccetti, S., & Cavaliere, A. 2008, *ApJ*, 686, 219
- Menéndez-Delmestre, K., Blain, A. W., Swinbank, M., et al. 2013, *ApJ*, 767, 151
- Merlin, E., Fontana, A., Ferguson, H. C., et al. 2015, *A&A*, 582, A15
- Merloni, A., Bongiorno, A., Brusa, M., et al. 2014, *MNRAS*, 437, 3550
- Momcheva, I. G., Brammer, G. B., van Dokkum, P. G., et al. 2015, *ApJ*, 225, 27
- Mullaney, J. R., Pannella, M., Daddi, E., et al. 2015, *MNRAS*, 453, L83
- Nanni, R., Vignali, C., Gilli, R., et al. 2017, *A&A*, 603, A128
- Nesvadba, N. P. H., Polletta, M., & Lehnert, M. D. 2011, *MNRAS*, 415, 2359
- Nesvadba, N., Kneissl, R., Cañameras, R., et al. 2016, *A&A*, 593, L2
- Nguyen, H. T., Schulz, B., Levenson, L., et al. 2010, *A&A*, 518, L5
- Ordovás-Pascual, I., Mateos, S., Carrera, F. J., et al. 2017, *MNRAS*, 469, 693
- Perna, M., Brusa, M., Cresci, G., et al. 2015a, *A&A*, 574, A82
- Perna, M., Brusa, M., Salvato, M., et al. 2015b, *A&A*, 583, A72
- Perna, M., Lanzuisi, G., Brusa, M., Mignoli, M., & Cresci, G. 2017, *A&A*, 603, A99
- Perna, M., Curti, M., & Cresci, G. et al. 2018, *A&A*, 618, A36
- Peterson, B. M., Wanders, I., Horne, K., et al. 1998, *PASP*, 110, 660
- Piconcelli, E., Vignali, C., Bianchi, S., et al. 2015, *A&A*, 574, L9
- Planck Collaboration XIII (Ade, P. A. R., et al.) 2016, *A&A*, 594, A13
- Podigachoski, P., Barthel, P. D., Haas, M., et al. 2015, *A&A*, 575, A80
- Polletta, M., Nesvadba, N. P. H., & Neri, R. 2011, *A&A*, 533, A20
- Popping, G., Decarli, R., Man, A. W. S., et al. 2017, *A&A*, 602, A11
- Prevot, M. L., Lequeux, J., Prevot, L., et al. 1984, *A&A*, 132, 389
- Press, W. H., Teukolsky, S. A., Vetterling, W. T., & Flannery, B. P. 1992, *Numerical recipes in Fortran*, 2nd ed
- Priddey, R. S., & McMahon, R. G. 2001, *MNRAS*, 324, 17
- Ricci, C., Trakhtenbrot, B., Koss, M. J., et al. 2017, *ApJ*, 233, 17
- Richards, G. T., Strauss, M. A., Fan, X., et al. 2006, *AJ*, 131, 2766
- Riechers, D. A., Walter, F., Carilli, C. L., et al. 2011, *ApJ*, 726, 50
- Riechers, D. A., Bradford, C. M., Clements, D. L., et al. 2013, *Nature*, 496, 329
- Roos, O., Juneau, S., Bournaud, F., & Gabor, J. M. 2015, *ApJ*, 800, 19
- Rosario, D., Burtscher, L., Davies, R. I., et al. 2018, *MNRAS*, 473, 5658
- Rupke, D. S. N., & Veilleux, S. 2013, *ApJ*, 775, 15
- Rupke, D. S. N., & Veilleux, S. 2015, *ApJ*, 801, 126
- Saintonge, A., Catinella, B., Cortese, L., et al. 2016, *MNRAS*, 462, 1749
- Saito, T., Iono, D., Ueda, J., et al. 2018, *MNRAS*, 475, 52
- Sanders, D. B., Soifer, B. T., Elias, J. H., et al. 1988, *ApJ*, 325, 74
- Santini, P., Maiolino, R., Magnelli, B., et al. 2014, *A&A*, 562, A30
- Sargent, M., Béthermin, M., Daddi, E., et al. 2012, *ApJ*, 747, 31
- Sargent, M., Daddi, E., Béthermin, M., et al. 2014, *ApJ*, 793, 19
- Schinnerer, E., Groves, B., Sargent, M. T., et al. 2016, *ApJ*, 833, 112
- Schumacher, H., Martínez-Sansigre, A., Lacy, M., et al. 2012, *MNRAS*, 423, 2132
- Scoville, N., Sheth, K., Aussel, H., et al. 2016, *ApJ*, 820, 83
- Shangguan, J., Ho, L. C., & Xie, Y. 2018, *ApJ*, 854, 158
- Sharon, C. E., Riechers, D. A., Hodge, H., et al. 2016, *ApJ*, 827, 18
- Shemmer, O., Brandt, W. N., Schneider, D. P., et al. 2006, *ApJ*, 644, 86
- Shi, Y., Helou, G., Yan, L., et al. 2011, *ApJ*, 733, 87
- Shields, G. A., Menezes, K. L., Massart, C. A., & Vanden, Bout P. 2006, *ApJ*, 641, 683
- Siemiginowska, A., LaMassa, S., Aldcroft, T. L., et al. 2008, *ApJ*, 684, 811
- Silk, J. 2013, *ApJ*, 772, 112
- Silva, L., Maiolino, R., & Granato, G. L. 2004, *MNRAS*, 355, 973
- Silverman, J. D., Daddi, E., Rodighiero, G., et al. 2015, *ApJ*, 812, L23
- Speagle, J. S., Steinhardt, C. L., Capak, P. L., & Silverman, J. D. 2014, *ApJS*, 214, 15
- Spilker, J. S., Bezanson, R., Marrone, D. P., et al. 2016, *ApJ*, 832, 19
- Solomon, P. M., & Vanden Bout, P. A. 2005, *ARA&A*, 43, 677
- Somerville, R. S., & Davé, R. 2015, *ARA&A*, 53, 51
- Stefan, I. I., Carilli, C. L., Wagg, J., et al. 2015, *MNRAS*, 451, 1713
- Stevens, J. A., Page, M. J., Ivison, R. J., et al. 2005, *MNRAS*, 360, 610
- Streblyanska, A., Barcons, X., Carrera, F. J., & Gil-Merino, R. 2010, *A&A*, 5151, A2
- Sturm, E., González-Alfonso, E., Veilleux, S., et al. 2011, *ApJ*, 733, L16
- Swinbank, M., Chapman, S. C., Smail, I., et al. 2006, *MNRAS*, 371, 465
- Symeonidis, M. 2017, *MNRAS*, 465, 1401
- Szokoly, G. P., Bergeron, J., Hasinger, G., et al. 2004, *ApJ*, 155, 271
- Tacconi, L. J., Neri, R., Genzel, R., et al. 2013, *ApJ*, 768, 74
- Tacconi, L. J., Genzel, R., Saintonge, A., et al. 2018, *ApJ*, 853, 179
- Talia, M., Pozzi, F., Vallini, L., et al. 2018, *MNRAS*, 476, 3956
- Trakhtenbrot, B., Lira, P., Netzer, H., et al. 2017, *ApJ*, 836, 8
- Ueda, Y., Hatsukade, B., Kohno, K., et al. 2018, *ApJ*, 853, 24
- Ursini, F., Bassani, L., Panessa, F., et al. 2017, *MNRAS*, 474, 5684
- Valiante, R., Schneider, R., Salvadori, S., & Gallerani, S. 2014, *MNRAS*, 444, 2442
- Vayner, A., Shelley, A. W., Murray, N., et al. 2017, *ApJ*, 851, 126
- Veilleux, S., Bolatto, A., Tombesi, F., et al. 2017, *ApJ*, 843, 18
- Venemans, B. P., Walter, F., Decarli, R., et al. 2017, *ApJ*, 845, 154
- Vignali, C., Brandt, W. N., Schneider, D. P., & Kaspi, S. 2005, *AJ*, 129, 2519
- Vignali, C., Alexander, D. M., Gilli, R., & Pozzi, F. 2010, *MNRAS*, 404, 48
- Vignali, C., Piconcelli, E., Perna, M., et al. 2018, *MNRAS*, 780, 790
- Vito, F., Brandt, W. N., Stern, D., et al. 2017, *MNRAS*, 474, 4528
- Wang, R., Carilli, C. L., Neri, R., et al. 2010, *ApJ*, 714, 699
- Wang, R., Wagg, J., Carilli, C. L., et al. 2011a, *ApJL*, 739, 34
- Wang, R., Wagg, J., Carilli, C. L., et al. 2011b, *AJ*, 142, 101
- Wang, R., Wagg, J., Carilli, C. L., et al. 2013, *ApJ*, 773, 44
- Wang, R., Wu, X., Neri, R., et al. 2016, *ApJ*, 830, 53
- Wardlow, J. L., et al. 2011, *MNRAS*, 415, 1479
- Whitaker, K. E., van Dokkum, P. G., Brammer, G., & Franx, M. 2012, *ApJ*, 754, 29
- Willott, C. J., Martínez-Sansigre, A., & Rawlings, S. 2007, *AJ*, 133, 567
- Yan, L., Tacconi, L. J., Fiolet, N., et al. 2010, *ApJ*, 714, 100
- Yang, C., Omont, A., Beelen, A., et al. 2017, *A&A*, 608, A114
- Young, M., Elvis, M., & Risaliti, G. 2009, *ApJS*, 183, 17
- Zakamska, N. L., Lampayan, K., Petric, A., et al. 2016, *MNRAS*, 455, 4191
- Zubovas, K., & King, A. R. 2014, *MNRAS*, 439, 400

Table A.1. Far-IR photometric data.

Band	BzK4892	BzK8608	CDF153
$S_{70\mu\text{m}}$	2.32 ± 0.02	<0.73	0.65 ± 0.20
$S_{100\mu\text{m}}$	5.64 ± 0.2 (5.67)	<0.72	2.56 ± 0.10
$S_{160\mu\text{m}}$	13.71 ± 0.2 (12.4)	1.23 ± 0.36	3.56 ± 0.19
$S_{250\mu\text{m}}$	25.88 ± 1.29 (20.0)	2.32 ± 0.62	–
$S_{350\mu\text{m}}$	25.07 ± 0.62 (17.2)	2.39 ± 0.69	–
$S_{500\mu\text{m}}$	15.23 ± 1.02 (16.3)	<1.59	–
$\log(L_{\text{IR}})$	12.80 ± 0.01 (12.43)	$11.42^{+0.34}_{-0.70}$ (12.26)	$11.70^{+0.04}_{-0.07}$ (12.00)

Notes. Far-IR photometric fluxes (in mJy) from T. Wang et al. (in prep.); 3σ upper limits are reported for $S_{70\mu\text{m}}$, $S_{100\mu\text{m}}$, and $S_{500\mu\text{m}}$ of BzK8608. CDF153 SPIRE data are not reported as the Wang et al. procedure was not able to recover reliable measurements. For BzK4892, we also report in parentheses the photometric fluxes from the CANDELS Rainbow Cosmological Surveys database. No Rainbow measurements are reported for BzK8608 and CDF153. In the last row we also report the (8–1000) μm IR luminosities derived in this work and those from the Rainbow database.

Appendix A: Far-IR photometry and SED fit comparison with previous works

The three obscured AGN presented in this work, BzK4892, BzK8608, and CDF153, have been observed as part of the GOODS-*Herschel* (Elbaz et al. 2011) and PEP (Magnelli et al. 2013) surveys. However, their PACS 70, 100, and 160 μm , and SPIRE 250, 350, and 500 μm photometric data may be affected by source confusion. To derive their host galaxy properties, we therefore used a new *Herschel* catalogue presented by T. Wang et al. (in prep.), which utilises an optimised algorithm (T-PHOT; Merlin et al. 2015) for photometry in crowded *Herschel* maps. T-PHOT uses minimum chi-square estimation to generate flux density estimates using galaxy positions extracted from shorter wavelength images.

In Table A.1 we report the T-PHOT fluxes used in this work and, when available, those from the Rainbow Cosmological Surveys database¹¹ for comparison.

BzK4892, BzK8608, and CDF153 multiband SED fits are also presented in the Rainbow database. However, for CDF153 and BzK8608 the SED fits were performed excluding the unblended, and hence potentially biased, $\lambda > 24\mu\text{m}$ photometry in the Rainbow database. Furthermore, in the Rainbow SED fits only stellar SED templates are used to reproduce the photometry. As a result, the L_{IR} and SFR measurements of these two sources cannot be compared with our measurements (Sect. 2.1). We also note that the Rainbow photometric redshift of BzK8608 is $z = 2.63$, while in this work we used $z = 2.51$. The Rainbow BzK4892 SED is instead also sampled in the far-IR, and their L_{IR} is compatible with our SED fit measurement within a factor of 2 (see also Elbaz et al. 2018). The stellar masses derived for the three targets are also compatible with ours within a factor of 2.

Appendix B: BzK8608 photometric redshift

We derived a photometric redshift for BzK8608 by running AGN-fitter on a grid of redshifts ($\Delta z = 0.01$) spanning the redshift range $2.4 < z < 3$, corresponding to the redshifts reported for BzK8608 in previous studies (e.g. Feruglio et al. 2011; Hsu et al. 2014). The normalised redshift likelihood distribution is shown in Fig. B.1;

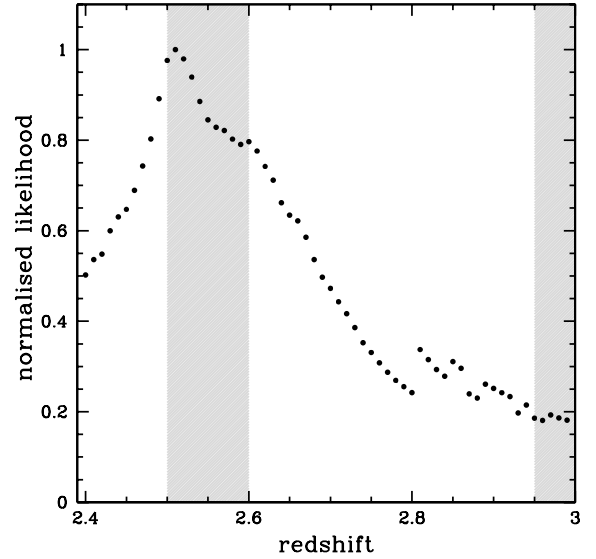


Fig. B.1. Likelihood distribution as a function of redshift, obtained repeating the SED fit computation of BzK8608 for fixed z value (the redshift binning is 0.01). The maximum corresponds to the redshift $z = 2.51$. Shaded areas represent the frequency coverage of our JVLA observations.

the adopted redshift $z_{\text{phot}} = 2.51^{+0.16}_{-0.06}$ corresponds to the peak of the distribution (redshift errors define the likelihood ratio limits at a 68% confidence interval; D’Agostini 2003). This redshift estimate is also consistent with the photometric redshift reported in Hsu et al. (2014).

Tentative spectroscopic redshifts from the iron $K\alpha$ line in X-ray spectra have been reported by (Feruglio et al. 2011, $z_{K\alpha} = 2.9 \pm 0.1$) and (Buchner et al. 2014, $z_{K\alpha} = 2.83 \pm 0.02$). However, this feature is not detected in the deeper *Chandra* observations (see Sect. 2).

The frequency coverage of our JVLA observations maps is in the two redshift intervals [2.5–2.6] and [2.95–3.08]. We searched for line emission through the accessible redshift range, finding no significant features. Given that an unambiguous spectroscopic redshift has not yet been obtained for this target, we used the derived photometric redshift for the estimate of the CO luminosity upper limit of BzK8608 and the host galaxy properties. We note that the IR luminosity and stellar mass derived with AGN-fitter do not show a significant dependence on redshift in the range $2.4 < z < 3$.

Appendix C: SMG and QSO samples

In Table C.1, C.2, and C.3 we reported the information collected from the literature for SMGs, obscured and unobscured AGN, respectively. Stellar masses, X-ray luminosities, and column densities are reported for the only sources for which these quantities have been reported in literature. All luminosities are re-derived using the values tabulated in the papers mentioned in Sect. 3 and considering Planck Collaboration XIII (2016) Cosmological parameters; the host galaxy quantities, instead, have been corrected for the adopted Chabrier IMF. Moreover, we tabulated measurement uncertainties (at the 1σ confidence level) for the only sources for which these quantities were previously reported in the literature. The stellar mass measurements of unobscured AGN are not reported in Table C.3 (see Sect. 4.2). Gas masses are tabulated for SMGs and dusty

¹¹ http://rainbow.fis.ucm.es/Rainbow_Database/Home.html

AGN targets, and are used to derive the gas fractions shown in Fig. 5.

The SMG/QSO sources presented in Coppin et al. (2008) and Bothwell et al. (2013) have been included in the obscured (dusty) AGN sample table (see Sect. 4.1). The dusty AGN are characterised by red spectra/colours (e.g. Banerji et al. 2017; Brusa et al. 2018; Coppin et al. 2008; Fan et al. 2018; Kakkad et al. 2017; Yan et al. 2010) and/or high column densities (e.g. Bothwell et al. 2013; Gilli et al. 2014; Polletta et al. 2011; Stefan et al. 2015; Vayner et al. 2017).

All the non-lensed luminous AGN are characterised by bright UV emission (with rest-frame absolute magnitude at 1450\AA of $M_{1450} < -25$; Bañados et al. 2016; Priddey & McMahon 2001), while lensed galaxies are all associated with negligible obscuration ($E(B - V) \lesssim 0.1^{12}$) and the presence of BLR emission lines in their rest-frame UV spectra (e.g. Anguita et al. 2008; Mazzucchelli et al. 2017; Sharon et al. 2016; Shields et al. 2006; Wang et al. 2013). The sample of unobscured AGN do not include the bright sources for which the IR luminosities are not available (e.g. Carniani et al. 2017).

We would like point out that only a few optically bright QSOs have been studied through their X-ray emission and that their characterisation requires long-exposure observations. Therefore, we cannot confidently exclude the presence of nuclear obscuration in the individual targets reported in Table C.3. We note, however, that there are several indications suggesting that the population of optically luminous QSOs are associated with X-ray spectra characterised by low column densities ($N_{\text{H}} \lesssim 10^{22} \text{ cm}^{-2}$; Nanni et al. 2017; Shemmer et al. 2006; Vignali et al. 2005). Therefore, we can be reasonably confident about the separation between the dusty and unobscured QSO populations presented in this work.

In Fig. C.1 we report the distribution of the stellar masses of star-forming galaxies and dusty AGN; these sources are associated with massive host galaxies, with an average $\langle M_{\text{star}} \rangle = 10^{11} M_{\odot}$. In Fig. C.1 (bottom panel) we also report the distribution of specific star formation ratio $\text{sSFR}/\text{sSFR}_{\text{MS}}$ (according to the relation of Speagle et al. 2014) for the same sources, showing that the majority of SFGs and dusty AGN collected in this work are associated with MS galaxies, with the latter population showing slightly higher MS-offsets $\text{sSFR}/\text{sSFR}_{\text{MS}}$.

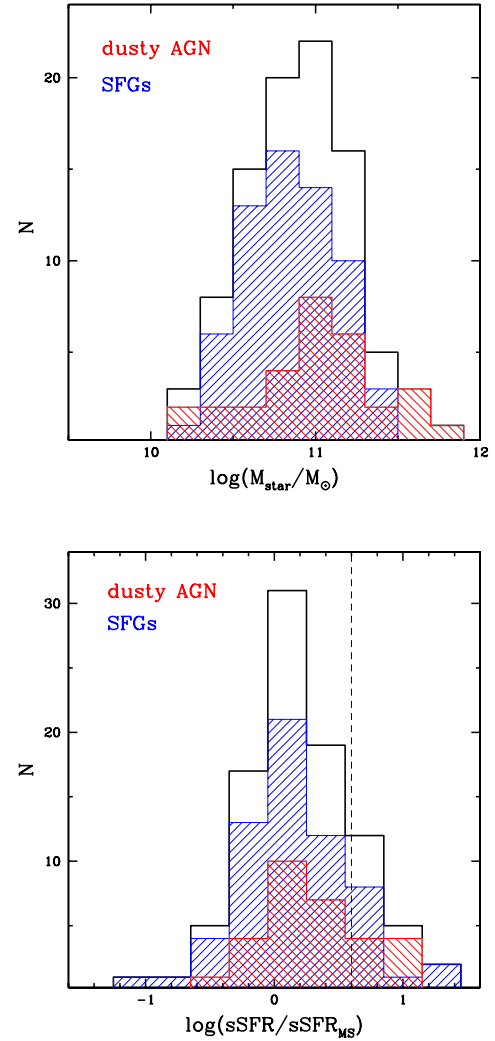


Fig. C.1. *Top panel:* stellar mass distribution for sample collected in this work. Blue- and red-shaded histograms refer to the samples of SFGs (i.e. MS and SMGs) and dusty AGN. *Bottom panel:* specific star formation rate $\text{sSFR}/\text{sSFR}_{\text{MS}}$ distributions for the same samples in the *top panel*. The sSFR_{MS} is derived according to the relation of Speagle et al. (2014). In the figure, we also show the separation between normal MS galaxies and SBs at $\log(\text{sSFR}/\text{sSFR}_{\text{MS}}) = 0.6$.

¹² <https://www.cfa.harvard.edu/castles/>

Table C.1. SMG sample.

Target	RA & Dec (J2000)	z	J_{up}	$r_{J_{\text{up}},1}$	L'_{CO} ($10^{10} \text{ K km s}^{-1} \text{ pc}^2$)	M_{gas} ($10^{10} M_{\odot}$)	$\log(M_{\text{star}})$ (M_{\odot})	$\log(L_{\text{IR}})$ (L_{\odot})	ref
(1)	(2)	(3)	(4)	(5)	(6)	(7)	(8)	(9)	(10)
SGP-196076	00:03:07 –33:02:50	4.425	4	0.41	38.83 ± 3.8	$31.1 \pm 3.0^{\circ}$		13.44	F17
SMMJ021725	02:17:25 –04:59:34	2.292	4	0.41	4.7 ± 0.5	$4.7 \pm 0.5^{\square}$		12.67	Bo13
SMMJ021738-050339	02:17:38 –05:03:39	2.037	4	0.41	11.0 ± 3.1	$11.0 \pm 3.1^{\square}$		12.67	Bo13
SMMJ021738-050528	02:17:38 –05:05:28	2.541	4	0.41	9.4 ± 2.9	$9.4 \pm 2.9^{\square}$		12.66	Bo13
ADFS-27	04:36:57 –54:38:10	5.655	5	0.32	35.9 ± 2.1	$28.7 \pm 1.7^{\circ}$		13.46	F17
SMMJ044315	04:43:07 +02:10:23	2.509	3	0.52	12.1 ± 3.5	$12.1 \pm 3.5^{\square}$		12.50	Bo13
J044307+0210	04:43:05+02:09:06	2.509	1	1.00	1.48 ± 0.40	$1.18 \pm 0.32^{\circ}$		12.17 ± 0.10	S16
J04135+10277	04:13:27 +10:27:43	2.846	1	1.00	8.4 ± 1.7	$6.7 \pm 1.4^{\circ}$		13.24 ± 0.05	S16
G09-81106	08:49:36 +00:14:54	4.531	4	0.41	15.3 ± 2.5	$12.2 \pm 2^{\circ}$		13.39	F17
SMMJ094303	09:43:03 +47:00:15	3.346	4	0.41	7.1 ± 1.6	$7.1 \pm 1.6^{\square}$		13.25	Bo13
PACS867	09:59:38 +02:28:56	1.566	2	0.85	2.03 ± 0.16	$2.23 \pm 0.18^{\bullet}$	10.67	12.62 ± 0.04	S15
PACS299	09:59:41 +02:14:42	1.645	2	0.85	3.21 ± 0.35	$3.53 \pm 0.38^{\bullet}$	10.44	12.81 ± 0.03	S15
PACS819	09:59:55 +02:15:11	1.445	2	0.85	4.15 ± 0.23	$2.49 \pm 1.2^{\dagger}$	10.61	12.96 ± 0.01	S15
PACS282	10:00:01 +02:11:24	2.187	3	0.70	3.20 ± 0.46	$3.52 \pm 0.51^{\bullet}$	10.88	12.83 ± 0.03	S15
PACS325	10:00:05 +02:19:42	1.656	2	0.85	1.67 ± 0.26	$1.84 \pm 0.28^{\bullet}$	10.29	12.21 ± 0.03	S15
PACS830	10:00:08 +02:19:01	1.463	2	0.85	4.55 ± 0.35	$7.3 \pm 2.2^{\dagger}$	10.86	12.78 ± 0.01	S15
AzTEC-3	10:00:20 +02:35:22	5.299	2	sled	7.6	6.1°		13.1	F17
PACS164	10:01:30 +01:54:12	1.648	2	0.85	2.93 ± 0.47	$3.22 \pm 0.50^{\bullet}$	>10.28	12.62 ± 0.01	S15
SMMJ105141	10:51:41 57:19:52	1.214	2	0.84	6.55 ± 0.52	$6.55 \pm 0.52^{\square}$		12.69	Bo13
SMMJ105151	10:51:51 +57:26:35	1.597	2	0.84	2.64 ± 1.45	$2.64 \pm 1.45^{\square}$	11.16	12.54	Bo13
SMMJ105227	10:52:27 +57:25:16	2.443	3	0.52	2.87 ± 0.61	$2.87 \pm 0.61^{\square}$	11.24	12.82	Bo13
SMMJ105307	10:53:07 +57:24:31	1.524	2	0.84	2.21 ± 0.31	$2.21 \pm 0.31^{\square}$		12.21	Bo13
SMMJ123549	12:35:49 +62:15:37	2.202	3	0.52	8.99 ± 0.72	$8.99 \pm 0.71^{\square}$	11.20	12.71	Bo13
SMMJ123555	12:35:55 +62:09:02	1.864	2	0.84	4.67 ± 1.54	$4.67 \pm 1.54^{\square}$	11.11	13.0	Bo13
SMMJ123634	12:36:34 +62:12:41	1.225	2	0.84	3.95 ± 0.42	$3.95 \pm 0.42^{\square}$	10.82	12.61	Bo13
GN 20	12:37:11 +62:22:11	4.055	2	1.0	18.7 ± 5.2	$15.0 \pm 4.2^{\circ}$	11.36	13.52	F17
SMMJ123712	12:37:12 +62:13:26	1.996	3	0.52	5.4 ± 1.4	$5.4 \pm 1.4^{\square}$	11.19	12.46	Bo13
SMMJ131201	13:12:01 +42:42:08	3.408	4	0.41	14.95 ± 3.8	$14.95 \pm 3.8^{\square}$	10.96	12.96	Bo13
NGP-284357	13:32:51 +33:23:42	4.894	6	0.21	30.2 ± 6.1	$24.2 \pm 4.9^{\circ}$		13.14	F17
NGP-246114	13:41:14 +33:59:38	3.847	4	0.41	14.3 ± 1.8	$11.4 \pm 1.4^{\circ}$		13.21	F17
SMMJ163658+405728	16:36:50 +40:57:34	1.193	2	0.84	2.2 ± 0.4	$2.2 \pm 0.4^{\square}$	10.89	12.09	Bo13
SMMJ163658+410523	16:36:58 +41:05:24	2.454	3	0.52	9.5 ± 1.0	$9.5 \pm 1.0^{\square}$	11.01	12.90	Bo13
MIPS506	17:11:38 +58:38:36	2.470	3	1.0	1.61 ± 0.34	$1.29 \pm 0.28^{\circ}$		12.92	Y10
MIPS16144	17:24:21 +59:31:51	2.131	3	1.0	4.05 ± 0.95	$3.24 \pm 0.74^{\circ}$		12.75	Y10
SMMJ221804	22:18:04 +00:21:54	2.517	3	0.52	9.96 ± 1.12	$9.96 \pm 1.12^{\square}$	10.79	12.53	Bo13
J22174+0015	22:17:34 +00:15:33	3.099	1	1.00	4.3 ± 1.0	$4.3 \pm 1.0^{\square}$	10.51	12.66 ± 0.11	S16
Lensed galaxies									
J083051.0+013224	08:30:51 +01:32:24	3.634	3	0.17	10.0 ± 4.4	$8.0 \pm 3.5^{\circ}$		13.11 ± 0.12	Y17
J085358.9+015537	08:53:58 +01:55:37	2.092	2	0.84	2.3 ± 0.9	$1.8 \pm 0.7^{\circ}$		12.39 ± 0.19	Y17
J090302.9-014127	09:03:03 –01:41:27	2.304	3	0.17	7.8 ± 2.1	$6.2 \pm 1.67^{\circ}$		12.92 ± 0.17	Y17
J090311.6+003906	09:03:11 +00:39:06	3.042	3	0.17	5.7 ± 1.5	$46 \pm 1.2^{\circ}$		12.48 ± 0.12	Y17
J114637.9–001132	11:46:37 –00:11:31	3.259	4	0.41	8.3 ± 2.4	$6.6 \pm 1.9^{\circ}$		12.97 ± 0.12	Y17
HDF 850.1	12:36:51 +62:12:25	5.183	2	sled	4.6	3.7°		12.83	F17
J125632.7+233625	12:56:32 +23:36:27	3.565	3	0.17	5.7 ± 1.5	$4.6 \pm 1.2^{\circ}$		12.82 ± 0.15	Y17
J133008.4+245900	13:30:08 +24:58:59	3.111	5	0.32	2.4 ± 0.6	$1.9 \pm 0.5^{\circ}$		12.68 ± 0.16	Y17
J133649.9+291801	13:36:49 +29:18:01	2.202	3	0.17	5.8 ± 1.6	$4.6 \pm 1.3^{\circ}$		12.89 ± 0.26	Y17
J134429.4+303036	13:44:29 +30:30:34	2.301	5	0.32	5.5 ± 1.1	$4.4 \pm 0.9^{\circ}$		12.75 ± 0.12	Y17
J141351.9–000026	14:13:51 –00:00:26	2.478	3	0.17	28.8 ± 7.6	$23.0 \pm 6.8^{\circ}$		12.95 ± 0.13	Y17
G15v2.779	14:24:13 +02:23:04	4.243	4	0.41	18.0 ± 4.3	$14.4 \pm 3.4^{\circ}$		13.10 ± 0.14	Y17
HFLS3	17:06:47 +58:46:23	6.337	1	1.0	9.49 ± 3.13	$9.49 \pm 3.13^{\square}$	10.57	13.45 ± 0.05	F17

Notes. Column (1): target name; Column (2): coordinates; Column (3): redshift; Column (4): J_{up} refers to the upper level of the ($J_{\text{up}} \rightarrow J_{\text{up}} - 1$) CO transition; Column (5): the excitation correction defined as $r_{J_{\text{up}},1} = \text{CO}(J_{\text{up}} \rightarrow J_{\text{up}} - 1) / \text{CO}(1 \rightarrow 0)$; Column (6): CO(1-0) luminosity; Column (7): gas mass; Column (8): stellar mass; Column (9): 8–1000 μm IR luminosity; Column (10): reference for the paper from which we derived CO and far-IR measurements, as well as assumed excitation correction and α_{CO} conversion factors. All lensed galaxy properties are corrected for magnification. The three lensed galaxies from [Fudamoto et al. \(2017\)](#), SGP-261206, NGP- 190387, and G09-83808, are not included in our sample as their magnification factors are unknown. The S15 and Y17 infrared luminosities are derived from SFR, using the following prescription: $L_{\text{IR}} = \text{SFR} \times 10^{10} L_{\odot}$ ([Kennicutt 1998](#), correcting for a Chabrier IMF). The luminosity-to-gas-mass conversion factors used to derive the gas mass in the different papers are indicated in the table as follows: \square : $\alpha_{\text{CO}} = 1.0$; \circ : $\alpha_{\text{CO}} = 0.8$; \bullet : $\alpha_{\text{CO}} = 1.1$; \dagger : the gas masses are derived from a CO-based dynamical mass estimate by subtracting stellar and dark matter components ([Silverman et al. 2015](#)). The inferred M_{gas} yielded the estimate of $\alpha_{\text{CO}} = 0.6 \pm 0.3$ (PACS819) and $\alpha_{\text{CO}} = 1.6 \pm 0.6$ (PACS830).

References. [Bothwell et al. \(2013, Bo13\)](#); [Fudamoto et al. \(2017, F17\)](#); [Sharon et al. \(2016, S16\)](#); [Silverman et al. \(2015, S15\)](#); [Yan et al. \(2010, Y10\)](#); [Yang et al. \(2017, Y17\)](#).

Table C.2. obscured QSO sample.

Target	RA & Dec (J2000)	z	J_{up}	$r_{\text{up},1}$	L'_{CO} ($10^{10} \text{ K km s}^{-1} \text{ pc}^2$)	M_{gas} ($10^{10} M_{\odot}$)	$\log(M_{\text{star}})$ (M_{\odot})	$\log(L_{\text{IR}})$ (L_{\odot})	ref	N_{H} (10^{22} cm^{-2})	$\log(L_X)$ (erg s^{-1})	ref.
(1)	(2)	(3)	(4)	(5)	(6)	(7)	(8)	(9)	(10)	(11)	(12)	(13)
no.682	03:32:59 -27:45:22	1.155	2	0.8	<0.84	<3.02*	10.6	11.92	K17	<1	42.43	Lu17
W0410-0913	04:10:10 -09:13:05	3.592	4	0.87	16.28 ± 1.44	$13.1 \pm 1.15^{\circ}$		13.72 ± 0.03	F18	–	<46.08	V17
X2522	09:57:28 +02:25:42	1.532	2	0.8	<1.67	<6.00*	11.3	12.5	K17	<0.8	45.03	M16
X5308	09:59:22 +01:36:18	1.285	2	0.8	<1.06	<3.82*	11.0	12.02	K17	<2	44.28	M16
C1148	10:00:04 +02:13:07	1.563	2	0.8	<1.66	<5.98*	11.1	12.2	K17	>2.7	44.42	M16
COSMOS22995	10:00:17 +02:24:52	2.469	1	1.0	<1.3	<1.3 $^{\square}$	11.08	12.3	Sp16	33 ± 17	43.91	Br14
COSB011	10:00:38 +02:08:22	1.827	sled	–	5.89 ± 1.16	$4.71 \pm 0.93^{\circ}$		13.13	A08	$1 - 10$	44.02	A08
C152	10:00:39 +02:37:19	1.188	2	0.8	<0.53	<1.91*	10.4	11.52	K17	<2.6	43.9	M16
C92	10:01:09 +02:22:55	1.581	2	0.8	2.64 ± 0.25	$9.5 \pm 0.9^*$	11.2	12.8	K17	$3.5^{+1.8}_{-1.5}$	43.73	M16
C103	10:01:10 +02:27:17	1.433	2	0.8	<0.66	<2.38*	10.7	11.82	K17	<1.6	44.15	M16
C1591	10:01:43 +02:33:31	1.238	2	0.8	1.67 ± 0.4	$6.0 \pm 1.4^*$	11.3	12.62	K17	$26.4^{+15}_{-3.1}$	44.25	M16
C488	10:01:47 +02:02:37	1.171	2	0.8	<0.42	<1.51*	10.3	11.62	K17	$4.3^{+2.0}_{-3.1}$	44.25	M16
XID2028	10:02:11 +01:37:06	1.592	sled	–	1.43 ± 0.63	$1.14 \pm 0.50^{\circ}$	11.65 ± 0.35	$12.47^{+0.01}_{-0.05}$	B18	0.7 ± 0.02	45.32	P15
HS1002	10:05:17 +43:46:09	2.102	1	1.0	11.9 ± 3.4	$9.5 \pm 2.7^{\circ}$		13.08 ± 0.08	C08,S16			
SDSS J1148+5251	11:48:16 +52:51:50	6.418	2	1.0	3.2 ± 0.3	$2.6 \pm 0.2^{\circ}$		13.16	St15	20^{+20}_{-15}	45.18 ± 0.12	G17
RXJ121803	12:18:04 +47:08:51	1.742	2	1.0	<2.47	<1.97*		12.8 ± 0.4	C08	$2^{+0.6}_{-1.0}$		S05
ULASJ1234	12:34:27 +09:07:54	2.503	3	0.8	4.4 ± 0.8	$3.5 \pm 0.6^{\circ}$		13.24 ± 0.12	Ba17	0.89 ± 0.09	45.13	Ba14
SMMJ123606	12:36:06 +62:10:24	2.505	3	0.52	2.86 ± 0.82	$2.86 \pm 0.82^{\square}$	10.3	12.81	Bo13	81^{+97}_{-42}	43.52	L10
SMMJ123618	12:36:18 +62:15:51	1.996	4	0.41	4.6 ± 0.6	$4.6 \pm 0.6^{\square}$	10.7	12.9	Bo13	<7.4		L10
SMMJ123707	12:37:07 +62:14:08	2.487	3	0.52	6.53 ± 1.53	$6.53 \pm 1.53^{\square}$	10.8	12.59	Bo13	$32.6^{+15.2}_{-13.8}$	43.50	L10
SMMJ123711	12:37:11 +62:13:31	1.995	3	0.52	8.2 ± 1.7	$8.2 \pm 1.7^{\square}$	11.5	12.83	Bo13	$67.1^{+41.8}_{-23.2}$	43.36	L10
SMMJ1237	12:37:16 +62:03:23	2.057	3	1.0	<0.62	<0.5 $^{\circ}$		12.71 ± 0.4	C08	0.17	44.02	Y09
RXJ1249	12:49:13 -05:59:19	2.240	1	1.0	5.1 ± 1.2	$4.1 \pm 1.0^{\circ}$		12.84 ± 0.08	C08,S16	$0.76^{+0.36}_{-0.32}$	44.92	S10
SMMJ1312	13:12:22 +42:38:13	2.554	3	1.0	1.2 ± 0.4	$1.0 \pm 0.3^{\circ}$		12.5 ± 0.4	C08	<1.26	44.6	Bo14
VCV J140955	14:09:55 +56:28:27	2.576	1	1.0	8.6 ± 2.3	$6.9 \pm 1.8^{\circ}$		13.31 ± 0.02	C08,S16			
3C 298	14:19:08 +06:28:35	1.438	3	0.97	1.15 ± 0.11	$0.92 \pm 0.09^{\circ}$		12.75 ± 0.01	Va17	21.4 ± 0.2	46.12	S08
ULASJ1539	15:39:10 +05:57:50	2.658	3	1.0	5.46 ± 0.94	$4.36 \pm 0.75^{\circ}$	10.9 ± 0.27	12.82	F14	4 ± 2	45.12	M17
J154359	15:43:59 +53:59:03	2.369	1	1.0	2.9 ± 0.7	$2.3 \pm 0.6^{\circ}$		12.86 ± 0.10	C08,S16	2	45.46	Y09
HS1611	16:12:39 +47:11:57	2.403	3	1.0	5.2 ± 0.8	$4.2 \pm 0.6^{\circ}$		13.1 ± 0.4	C08			
SMMJ163650	16:36:50 +40:57:34	2.383	3	0.52	11.4 ± 0.7	$11.4 \pm 0.7^{\square}$	11.0	13.24	Bo13			
MMJ163655	16:36:55 +40:59:10	2.607	3	1.0	<0.8	<0.6 $^{\circ}$		12.8 ± 0.4	C08	32 ± 6	44.89	M03
SMMJ163706	16:37:06 +40:53:15	2.377	3	0.52	3.8 ± 0.7	$3.8 \pm 0.7^{\square}$	11.1	12.76	Bo13			
J164914	16:49:14 +53:03:16	2.270	3	1.0	<2.2	<1.8 $^{\circ}$		12.9 ± 0.4	C08	<0.79	45.51	

Notes. *Molecular gas:* For each target we report the upper level of the CO transition, J_{up} , and the excitation correction, $r_{\text{up},1}$ (see Notes in Table C.1). For COSB011 and XID2028, the CO(1-0) luminosity was derived extrapolating the ground-state transition flux from the QSOs SLEDs. We also indicate the luminosity-to-gas-mass conversion factors used to derive the gas mass in the different papers, as follows: *: $\alpha_{\text{CO}} = 3.6$; \square : $\alpha_{\text{CO}} = 1.0$; $^{\circ}$: $\alpha_{\text{CO}} = 0.8$. The sample of dusty AGN comprises a large number of sources associated with evidence of multiphase outflows: broad and shifted components in the [O III] emission lines (e.g. Coppin et al. 2008; Perna et al. 2015a; Polletta et al. 2011) and in molecular CO lines (e.g. Banerji et al. 2017; Brusa et al. 2018; Fan et al. 2018; Stefan et al. 2015) are usually found in these targets. For a small number of sources there are also indications of ongoing mergers (W0149+2350, SMMJ030227, 3C 298). For these sources, characterised by complex CO line profiles, we report in the Table (and in the figures) the total molecular luminosities and masses obtained integrating over all the different kinematic components. *X-ray luminosities and Column densities:* X-ray luminosities refer to the 2–10 keV rest-frame absorption-corrected luminosities; column densities are derived from X-ray spectroscopic analysis for all but no. 226 and no. 682, for which N_{H} is derived from the hardness ratio, following the prescriptions in Elvis et al. (2012). To our knowledge, the only CT sources with molecular line observations are XID403 (from C10, G14), SW022513, and SW022550 (from P11), and GMASS953 (from T18). The source C1148 (from K17), detected with 20 net counts in X-ray, is a candidate CT source (see Sect. 4.1). The few CT sources at $z > 1$ are tabulated in the lower part of the table. *Stellar masses and IR luminosities:* A08, B18, E14, F18, G14, K17, St15 (from Leipski et al. 2013), St17, Po17 (from T18), Va17 (from Podigachoski et al. 2015), and Y10 host galaxy properties are obtained with a two-component (AGN+galaxy) SED fit; their IR luminosities refer therefore to the only stellar component. B13: IR luminosities are obtained from the 1.4 GHz continuum. Ba17: IR luminosities are obtained using a modified greybody model assuming dust temperature and dust emissivity values ($T = [41, 47]$; $\beta = [1.6, 1.95]$), and rescaling the model to match the 3mm observations. C08: stellar mass from Wardlow (2011); L_{IR} assuming a dust temperature of $T = 40$ K and a dust emissivity factor of ν^{β} , with $\beta = 1.5$, rescaling a modified greybody model to match the 850 or 1200 μm photometry. F14: stellar IR luminosity is obtained with a two-component (AGN+galaxy) SED fit, but is not well constrained due to the lack of data above the 22 μm . P11: stellar IR luminosities are obtained with a two-component (AGN+galaxy) SED fit, but is not well constrained due to the lack of data between 24 μm and 1.2mm. M_{star} from H-band luminosity. S12: IR luminosity is obtained by fitting the far-IR SED with a greybody model. Sp16: SFR and stellar mass from 3D-HST catalogue (Momcheva et al. 2015, i.e. without considering AGN component). The source is undetected in any *Herschel*/PACS or SPIRE bands. The infrared luminosity is derived from SFR, using the following prescription: $L_{\text{IR}} = \text{SFR} \times 10^{10} L_{\odot}$ (Kennicutt 1998, correcting for a Chabrier IMF). Y10: these sources are undetected in SPIRE bands; far-IR emission is constrained using upper limits and mid-IR *Spitzer* spectra. Column (1): target name; Column (2): coordinates; Column (3): redshift; Column (4): J_{up} refers to the upper level of the ($J_{\text{up}} \rightarrow J_{\text{up}} - 1$) CO transition; Column (5): the excitation correction defined as $r_{\text{up},1} = \text{CO}(J_{\text{up}} \rightarrow J_{\text{up}} - 1) / \text{CO}(1 \rightarrow 0)$; Column (6): CO(1-0) luminosity; Column (7): gas mass; Column (8): stellar mass; Column (9): 8–1000 μm IR luminosity; Column (10): reference for the paper from which we derived CO and far-IR measurements, as well as assumed excitation correction and α_{CO} conversion factors. Columns (11) and (12): column density and 2–10 keV rest-frame absorption-corrected luminosities derived from X-ray spectroscopic analysis (see below). Column (13): reference for the paper from which we derived X-ray properties.

References. Aravena et al. (2008, A08); Banerji et al. (2017, Ba17); Banerji et al. (2014, Ba14); Bauer et al. (2010, B10); Bothwell et al. (2013, Bo13); Bongiorno (2014, Bo14); Brightman et al. (2014, Br14); Brusa et al. (2018, B18); Coppin et al. (2008, C08); Coppin et al. (2010, C10); Della Mura et al. (in prep., DM); Emonts et al. (2014, E14); Fan et al. (2018, F18); Feruglio et al. (2014, F14); Gallerani et al. (2017, G17); Gilli et al. (2014, G14); Kakkad et al. (2017, K17); Laird et al. (2010, L10); Luo et al. (2017, Lu17); Marchesi et al. (2016, M16); Martocchia et al. (2017, M17); Perna et al. (2015a, P15); Polletta et al. (2011, P11); Popping et al. (2017, Po17); Siemiginowska et al. (2008, S08); Schumacher et al. (2012, S12); Sharon et al. (2016, S16); Spilker et al. (2016, Sp16); Stefan et al. (2015, St15); Stevens et al. (2005, S05); Streblyanska et al. (2010, S10); Talia et al. (2018, T18); Vayner et al. (2017, Va17); Vito et al. (2017, Vi17); Yan et al. (2010, Y10); Young et al. (2009, Y09).

Table C.2. continued.

Target	RA & Dec (J2000)	z	J_{up}	$r_{J_{\text{up},1}}$	L'_{CO} ($10^{10} \text{ K km s}^{-1} \text{ pc}^2$)	M_{gas} ($10^{10} M_{\odot}$)	$\log(M_{\text{star}})$ (M_{\odot})	$\log(L_{\text{IR}})$ (L_{\odot})	ref	N_{H} (10^{22} cm^{-2})	$\log(L_X)$ (erg s^{-1})	ref.
(1)	(2)	(3)	(4)	(5)	(6)	(7)	(8)	(9)	(10)	(11)	(12)	(13)
MIPS8342	17:14:11 +60:11:09	1.562	2	1.0	2.32 ± 0.25	$1.86 \pm 0.20^{\circ}$		12.56	Y10	–	<43.45	B10
MIPS8196	17:15:10 +60:09:54	2.586	3	1.0	<1.70	<1.36 $^{\circ}$		13.0	Y10	–	<43.78	B10
MIPS8327	17:15:35 +60:28:25	2.441	3	1.0	1.31 ± 0.21	$1.04 \pm 0.17^{\circ}$		12.84	Y10			
MIPS429	17:16:11 +59:12:13	2.213	3	1.0	2.97 ± 0.50	$2.38 \pm 0.40^{\circ}$		12.73	Y10			
AMS12	17:18:22 +59:01:54	2.767	3	1.0	4.4 ± 0.4	$3.5 \pm 0.3^{\circ}$	11.48 ± 0.04	13.52 ± 0.10	S12			
MIPS16080	17:18:44 +60:01:16	2.007	3	1.0	2.08 ± 0.37	$1.66 \pm 0.30^{\circ}$		12.72	Y10	–	<43.7	B10
MIPS15949	17:21:09 +60:15:01	2.122	3	1.0	2.79 ± 0.29	$2.23 \pm 0.23^{\circ}$		12.91	Y10			
MIPS16059	17:24:28 +60:15:33	2.326	3	1.0	1.80 ± 0.55	$1.44 \pm 0.43^{\circ}$		12.88	Y10			
VHSJ2101	21:01:19 –59:43:44	2.313	3	0.8	1.78 ± 0.11	$1.44 \pm 0.09^{\circ}$		12.93 ± 0.15	Ba17			
ULASJ2315	23:15:56 +01:43:50	2.560	3	0.8	4.31 ± 0.21	$3.44 \pm 0.16^{\circ}$		13.61 ± 0.03	Ba17	0.71 ± 0.44	45.52	M17
Compton Thick QSOs												
SW022513	02:25:13 –04:39:19	3.427	4	1.0	8.4 ± 1.2	$6.72 \pm 0.96^{\circ}$	11.3–11.6	12.5–13.3	P11	≥ 100	44.78	P11
SW022550	02:25:50 –04:21:49	3.867	4	1.0	5.8 ± 1.0	$4.64 \pm 0.80^{\circ}$	11.2–11.9	12.5–13.2	P11	≥ 100	<45.5	P11
XID403	03:32:29 –27:56:19	4.762	2	1.0	2.0 ± 0.4	$1.6 \pm 0.3^{\circ}$	10.8 ± 0.22	12.78 ± 0.07	G14	140 ± 70	44.40	G14
GMASS953	03:32:31 –27:46:23	2.225	3	0.1	2.1 ± 0.2	$1.7 \pm 0.1^{\circ}$	11.3 ± 0.1	12.33 ± 0.04	Pol17	340^{+370}_{-150}	43.61	DM

Table C.3. Optically bright QSO sample.

Target	RA & Dec (J2000)	z	J_{up}	$r_{J_{\text{up}},1}$	L'_{CO} ($10^{10} \text{ K km s}^{-1} \text{ pc}^2$)	$\log(L_{\text{IR}})$ (L_{\odot})	Ref.
(1)	(2)	(3)	(4)	(5)	(6)	(7)	(8)
LBQS0018-0220	00:21:27 -02:03:33	2.620	3	1.0	5.7 ± 0.99	13.54	S05
J0100+2802	01:00:13 +28:02:25	6.326	2	1.0	1.25 ± 0.49	12.54 ± 0.09	W16
J0109-3047	01:09:53 -30:47:26	6.791	6	0.78	1.35 ± 0.22	$12.13^{+0.07}_{-0.23}$	V17
SDSS J012958	01:29:58 -00:35:39	5.779	6	0.78	1.59 ± 0.33	12.75 ± 0.07	CW13
SDSSJ020332	02:03:32 +00:12:29	5.72	6	0.8	<1.31	12.64 ± 0.11	W11a
CFHQS J021013.19-045620.9	02:10:13-04:56:20	6.438	2	1.0	<1.28	<12.28	W11b
J0305-3150	03:05:16 -31:50:55	6.615	6	0.78	3.5 ± 0.3	$12.88^{+0.01}_{-0.19}$	V17
J033829	03:38:29 +00:21:56	5.027	5	1.0	2.7 ± 0.3	13.24	CW13
J083643.5+005453.3	08:36:43 +00:54:53	5.774	5	1.0	<1.9	<13.62	M07
J0840+5624	08:40:35 +56:24:20	5.844	5	0.88	3.2 ± 0.4	12.86*	CW13
J0911+0027	09:11:48 +00:27:18	2.372	3	1.0	2.81 ± 0.52	12.55 ± 0.1	CW13
J0908-0034	09:08:47 -00:34:16	2.551	3	1.0	1.2 ± 0.2	12.5 ± 0.1	CW13
J0927+2001	09:27:21 +20:01:23	5.7716	2	1.0	5.19 ± 0.72	13.02*	CW13
MRC0943-242	09:45:32 -24:28:50	2.923	1	1.0	8.45 ± 2.56	12.99	G16
BR 1033-0327	10:36:23 -03:43:19	4.509	5	1.0	<1.55	13.00	G99
J1044-0125	10:44:33 -01:25:02	5.844	6	0.78	0.8 ± 0.2	12.30*	CW13
J1048+4637	10:48:45 +46:37:18	6.227	6	0.78	1.2 ± 0.2	12.40*	CW13
PSS 1048+4407	10:48:46 +44:07:13	4.450	5	1.0	<1.17	13.11	G99
BR 1117-1329	11:20:10 -13:46:26	3.958	4	1.0	<2.17	13.28	G99
BR 1144-0723	11:46:35 -07:40:05	4.147	5	1.0	<1.49	13.00	G99
BR 1202-0725	12:05:23 -07:42:33	4.693	1	1.0	10.1 ± 0.4	13.35 ± 0.13	CW13
LBQS1230+1627B	12:33:10 +16:10:54	2.741	3	0.87	2.52 ± 0.82	13.26	CW13
ULAS J131911	13:19:11 +09:50:51	6.132	6	0.78	1.9 ± 0.4	13.0 ± 0.06	CW13
J1335+3533	13:35:50 +35:33:16	5.901	6	0.78	2.2 ± 0.3	12.58*	CW13
BRI 1335-0417	13:38:03 -04:32:35	4.407	2	1.0	9.62 ± 1.57	13.44	CW13
J1425+3254	14:25:16 +32:54:10	5.892	6	0.78	2.5 ± 0.5	12.65*	CW13
CFHQS J142952	14:29:52 +54:47:17	6.183	2	1.0	4.7 ± 0.5	12.83	CW13
3C 318	15:20:05 +20:16:06	1.577	2	0.8	4.1 ± 0.8	12.98	CW13
SDSS J162331.81+311200.5	16:23:31 +31:12:00	6.260	2	1.0	<2.0	<13.41	W11b
J163033.90+401209.6	16:30:33 +40:12:10	6.065	6	1.0	<1.0	<12.90	M07
PG1634+706	16:34:51 +70:37:37	1.337	2	1.0	<0.99	13.35	E98
J2054-0005	20:54:06 -00:05:15	6.038	6	0.78	1.5 ± 0.3	12.66*	CW13
J2310+1855	23:10:38 +18:55:20	6.002	6	0.78	4.2 ± 0.3	13.25 ± 0.05	W13
J2348-3054	23:48:33 -30:54:10	6.902	6	0.78	1.47 ± 0.21	$12.67^{+0.04}_{-0.22}$	V17

Notes. Most of the luminosity measurements are from (Carilli & Walter 2013, see their Supplemental Table for details) and Riechers et al. (2011); the luminosities marked with * are from Wang et al. (2010) and are corrected for AGN far-IR emission. V17, W11a, W13, and W16 infrared luminosities are derived from modified greybody models, while G16 L_{IR} is obtained from a two-component (AGN+galaxy) SED fit. The IR luminosities of G99 targets are taken from (Priddey & McMahon 2001, for the BR targets) and (Isaak et al. 2002, for PSS 1048+4407) and are obtained from modified greybody models; the CO(1-0) luminosity upper limits are here inferred by assuming $r_{J_{\text{up}},1} = 1$. W11b and E98 IR luminosities are taken from Lyu et al. (2016), and are obtained from a two-component (AGN+galaxy) SED fit. LBQS0018-0220 CO and IR luminosities are reported in Solomon & Vanden Bout (2005), but no further information is found in the literature for this target. Column (1): target name; Column (2): coordinates; Column (3): redshift; Column (4): J_{up} refers to the upper level of the ($J_{\text{up}} \rightarrow J_{\text{up}} - 1$) CO transition; Column (5): the excitation correction defined as $r_{J_{\text{up}},1} = \text{CO}(J_{\text{up}} \rightarrow J_{\text{up}} - 1) / \text{CO}(1 \rightarrow 0)$; Column (6): CO(1-0) luminosity; Column (7): gas mass; Column (8): 8–1000 μm IR luminosity; Column (9): reference for the paper from which we derived CO and far-IR measurements, as well as assumed excitation correction factors. All lensed galaxy properties are corrected for magnification.

References. Carilli & Walter (2013, CW13); Evans et al. (1998, E98); Guilloateau et al. (1999, G99); Gullberg et al. (2016, G16); Riechers et al. (2011, R11); Solomon & Vanden Bout (2005, S05); Venemans et al. (2017, V17); Wang et al. (2011a, W11a); Wang et al. (2011b, W11b); Wang et al. (2013, W13); Wang et al. (2016, W16).

Table C.3. continued.

		Lensed QSOs					
HE 0230–2130	02:32:33–21:17:26	2.166	3	0.98	1.51 ± 0.06	12.26	R11
J04135+10277	04:13:27 +10:27:40	2.846	3	0.98	18.1 ± 1.1	13.48	R11
MG 0414+0534	04:14:37 +05:34:42	2.639	3	0.98	0.35	12.17	R11
MG 0751+2716	07:51:41 +27:16:32	3.199	3	0.98	1.48 ± 0.05	12.58	R11
APM 08279+5255	08:31:41 +52:45:17	3.912	1	1.0	2.51 ± 0.09	12.44	R11
RX J0911+0551	09:11:27 +05:50:54	2.796	3	0.98	0.54 ± 0.02	12.46	R11
BRI 0952–0115	09:55:00 –01:30:07	4.434	5	0.88	0.78 ± 0.01	12.48	R11
Q 0957+561	10:01:20 +55:53:50	1.414	2	1.0	1.99 ± 0.04	12.75	R11
F10214+4724	10:24:34 +47:09:10	2.286	3	0.98	0.57 ± 0.02	12.64	R11
HE 1104–1805	11:06:33–18:21:23	2.322	3	0.98	2.09 ± 0.07	12.27	R11
BR 1202–0725	12:05:23–07:42:33	4.695	1	1.0	10.0 ± 0.4	13.35	R11
Cloverleaf	14:15:46 +11:29:44	2.558	3	0.98	4.26 ± 0.01	12.83	R11
B1359+154	14:01:35 +15:13:26	3.239	4	0.94	0.065 ± 0.001	11.07	R11
B 1938+666	19:38:25 +66:48:53	2.059	3	0.98	0.13 ± 0.01	11.28	R11
PSS J2322+1944	23:22:07 +19:44:23	4.119	1	1.0	2.00 ± 0.04	12.73	R11